

See discussions, stats, and author profiles for this publication at: <https://www.researchgate.net/publication/230723716>

# Direct Calculation of Li-Ion Transport in the Solid Electrolyte Interphase

ARTICLE in JOURNAL OF THE AMERICAN CHEMICAL SOCIETY · AUGUST 2012

Impact Factor: 12.11 · DOI: 10.1021/ja305366r · Source: PubMed

CITATIONS

59

READS

163

7 AUTHORS, INCLUDING:



Yue Qi

Michigan State University

110 PUBLICATIONS 2,489 CITATIONS

SEE PROFILE



Louis . Hector,

General Motors Company

194 PUBLICATIONS 3,495 CITATIONS

SEE PROFILE



Hong Li

Chinese Academy of Sciences

277 PUBLICATIONS 10,712 CITATIONS

SEE PROFILE



Stephen Joel Harris

University of California, Berkeley

110 PUBLICATIONS 4,228 CITATIONS

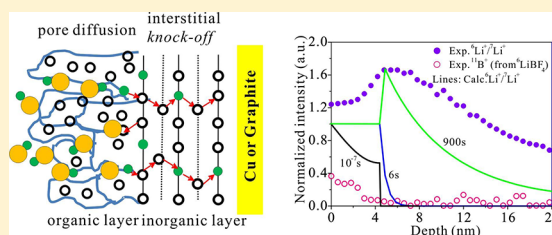
SEE PROFILE

## Direct Calculation of Li-Ion Transport in the Solid Electrolyte Interphase

Siqi Shi,<sup>†,||</sup> Peng Lu,<sup>‡</sup> Zhongyi Liu,<sup>§</sup> Yue Qi,<sup>\*,§</sup> Louis G. Hector, Jr.,<sup>§</sup> Hong Li,<sup>⊥</sup> and Stephen J. Harris<sup>§</sup><sup>†</sup>School of Engineering, Brown University, Providence, Rhode Island 02912, United States<sup>‡</sup>Trison Business Solutions Inc., 17 Bank Street, Le Roy, New York 14482, United States<sup>§</sup>General Motors R&D Center, Warren, Michigan 48090, United States<sup>⊥</sup>Institute of Physics, Chinese Academy of Sciences, Beijing 100190, China<sup>||</sup>Department of Physics, Zhejiang Sci-Tech University, Hangzhou 310018, China

## Supporting Information

**ABSTRACT:** The mechanism of Li<sup>+</sup> transport through the solid electrolyte interphase (SEI), a passivating film on electrode surfaces, has never been clearly elucidated despite its overwhelming importance to Li-ion battery operation and lifetime. The present paper develops a multiscale theoretical methodology to reveal the mechanism of Li<sup>+</sup> transport in a SEI film. The methodology incorporates the boundary conditions of the first direct diffusion measurements on a model SEI consisting of porous (outer) organic and dense (inner) inorganic layers (similar to typical SEI films). New experimental evidence confirms that the inner layer in the ~20 nm thick model SEI is primarily crystalline Li<sub>2</sub>CO<sub>3</sub>. Using density functional theory, we first determined that the dominant diffusion carrier in Li<sub>2</sub>CO<sub>3</sub> below the voltage range of SEI formation is excess interstitial Li<sup>+</sup>. This diffuses via a *knock-off* mechanism to maintain higher O-coordination, rather than *direct-hopping* through empty spaces in the Li<sub>2</sub>CO<sub>3</sub> lattice. Mesoscale diffusion equations were then formulated upon a new two-layer/two-mechanism model: pore diffusion in the outer layer and knock-off diffusion in the inner layer. This diffusion model predicted the unusual isotope ratio <sup>6</sup>Li<sup>+</sup>/<sup>7</sup>Li<sup>+</sup> profile measured by TOF-SIMS, which increases from the SEI/electrolyte surface and peaks at a depth of 5 nm, and then gradually decreases within the dense layer. With no fitting parameters, our approach is applicable to model general transport properties, such as ionic conductivity, for SEI films on the surface of other electrodes, from the atomic scale to the mesoscale, as well as aging phenomenon.



## 1. INTRODUCTION

Commercial Li-ion batteries, designed to last for more than 10 years, are actually operated under conditions where the non-aqueous electrolyte is thermodynamically unstable over a wide voltage range. Fortunately, continuous reduction of the non-aqueous electrolyte on the surface of the anode material (e.g., graphite) can be kinetically prevented by the formation of a solid electrolyte interphase (SEI) during the initial charging cycles. The SEI electronically isolates the negative electrode from the electrolyte but permits Li<sup>+</sup> transport from the electrolyte to the negative electrode, thereby enabling the battery to operate below the reduction voltage of the electrolyte.<sup>1–6</sup> The generally accepted picture of the electrochemically formed SEI is a mixture of organic materials [e.g., (CH<sub>2</sub>OCO<sub>2</sub>Li)<sub>2</sub> and ROLi (R is an organic group that depends on the solvent)] in an outer layer near the SEI/electrolyte interface and inorganic materials (e.g., Li<sub>2</sub>CO<sub>3</sub>, LiF, and Li<sub>2</sub>O) in an inner layer near the SEI/electrode interface.<sup>2–4,7</sup> Recent atomic force microscopy measurements further confirmed the existence of the two-layer structure in the SEI (on MnO anode) and illustrated that the two layers have different mechanical properties.<sup>8</sup> Even after the SEI is formed during the initial charging cycles, its chemistry and properties are

not generally fixed, but evolve over time and cycling. Battery properties, such as columbic efficiency, energy efficiency, rate performance, capacity retention, and durability, are highly dependent on SEI chemical, mechanical, and transport properties. However, its nanometric scale thickness (~10–100 nm, over electronic tunneling length) combined with its complex mosaic and heterogeneous structure have prompted Winter et al. to state that the SEI remains “the most important but the least understood in rechargeable Li batteries”.<sup>9–11</sup>

Numerous studies over the past four decades have been aimed at mechanistic understanding of SEI formation;<sup>2–6</sup> however, the mechanism of Li<sup>+</sup> transport through the SEI film from the electrolyte phase to the host lattice of the negative electrode has received only minimal attention. Active Li<sup>+</sup> is consumed in the SEI film, leading to irreversible capacity and capacity fade, while the rate of the “additional” transport step of Li<sup>+</sup> through the SEI contributes to the Li-ion battery power loss and fading.

The charge-transfer reaction on a SEI-covered electrode is thought to include at least three steps: the Li<sup>+</sup> desolvation step at

Received: June 14, 2012

Published: August 21, 2012

the SEI/electrolyte interface,  $\text{Li}^+$  diffusion through the SEI layer, and the electron-transfer step at the SEI/electrode interface or at the electrode active layer/current collector interface. In an early study by Peled<sup>12</sup> and a recent study by Xu et al.,<sup>13</sup> it was suggested that the  $\text{Li}^+$  diffusion process inside the SEI is rate-limiting for the overall charge-transfer reaction.

Despite the well-accepted heterogeneous nature of SEI film structure, all theoretical models of  $\text{Li}^+$  diffusion in the extant literature ignore its two-layer structure. Diffusion is assumed to occur through a homogeneous medium either through grain boundaries,<sup>14</sup> vacancies and interstitials,<sup>15</sup> or through a liquid of polar-ionic species.<sup>16</sup> However, previous studies lack experimental validation, and any theoretical analyses are often in question.

In tracer diffusion studies recently reported by Lu and Harris,<sup>17</sup> the SEI film was shown to be heterogeneous. In their experiments, a SEI film was formed on a Cu substrate using a  $^7\text{LiClO}_4$  electrolyte and subsequently soaked in a  $^6\text{LiBF}_4$  electrolyte for isotope exchange. The Cu substrate was chosen since it will not be lithiated, thereby enabling study only of the  $\text{Li}^+$  diffusion in the SEI. Time-of-flight secondary ion mass spectrometer (TOF-SIMS) depth profiles showed that the  $\text{BF}_4^-$  penetrated about 5 nm into the SEI, but the  $^6\text{Li}^+$  penetrated all the way through the  $\sim 20$  nm thick SEI film. The measured isotope ratio of  $^6\text{Li}^+/^7\text{Li}^+$  saturated quickly at the outer surface of the SEI but kept increasing in the inner part of the SEI. After a 15-min soak, the isotope ratio  $^6\text{Li}^+/^7\text{Li}^+$  inside the SEI became higher than that near the electrolyte/SEI interface. This unusual (climbing) concentration profile cannot be explained with any existing homogeneous SEI diffusion models. Such models would predict a  $^6\text{Li}^+/^7\text{Li}^+$  ratio that first decays with film thickness and then eventually converges to a constant value after equilibrium. Based on the Lu and Harris<sup>17</sup> experiments, the SEI formed on Cu substrate is composed of two layers. The outer layer is a 5 nm porous layer of organic materials, permeable to both  $\text{Li}^+$  and anions (dissolved in electrolyte), while the dense inner layer is not porous and is permeable only to  $\text{Li}^+$ . Furthermore, the dense layer acts as a rate-limiting “gateway” for  $\text{Li}^+$  transport through the SEI. Although the Lu and Harris<sup>17</sup> study provided important insights into the SEI structure on Cu anode, the structure of the dense inner layer as well as the mechanism of  $\text{Li}^+$  transport within it remain uncertain. Lu and Harris<sup>17</sup> proposed that the dense inner layer consists of either  $\text{Li}_2\text{O}$  or  $\text{Li}_2\text{CO}_3$  or both. Indeed, the dense phase of SEI films has been the point of some controversy in the literature. For example, Mizusaki et al.<sup>18</sup> claimed that crystalline  $\text{Li}_2\text{CO}_3$  was a pure lithium ion conductor, while others<sup>9</sup> have argued against its being an ionic conductor. As mentioned above,  $\text{Li}_2\text{CO}_3$  is the main component in carbonate-based nonaqueous electrolyte. In many reports, the observed SEI films on anode surfaces are amorphous. However, crystalline  $\text{Li}_2\text{CO}_3$  has been observed by TEM on a graphite anode surface after cycling,<sup>19,20</sup> and it has been suggested that  $\text{Li}_2\text{CO}_3$  is the material responsible for stabilizing the SEI.<sup>21</sup> Therefore, crystalline  $\text{Li}_2\text{CO}_3$  can be considered as a very suitable model material for simulating the transport of  $\text{Li}^+$  through the dense layer of SEI.

In the present paper, the mechanism of  $\text{Li}^+$  transport through the SEI film is elucidated through a combined theoretical/experimental approach. Specifically, a two-layer/two-mechanism model for  $\text{Li}^+$  transport is developed on the basis of insights provided by the recently published TOF-SIMS experiments<sup>17</sup> together with new SEI structural characterization reported herein. The latter is based upon TEM, HRTEM, and XPS analyses of SEI films grown under the Lu and Harris<sup>17</sup> experimental conditions

and confirms that the outer SEI layer is indeed a porous material, but the dense inner layer is primarily crystalline (monoclinic)  $\text{Li}_2\text{CO}_3$ . The theoretical component of this study is an integrated multiscale methodology which provides the means to directly compute  $\text{Li}^+$  diffusion in SEI on the basis of the two-layer structure of the SEI. The difference in structure between these two layers requires that  $\text{Li}^+$  transport occurs via two mechanisms. One is pore diffusion following Fick's law through the outer layer, while the other involves a previously unknown mechanism through the dense  $\text{Li}_2\text{CO}_3$  inner layer. A theoretical methodology that combines first-principles density functional theory (DFT), the climbing image nudged elastic band (CI-NEB) method, and the supercell approach to lattice dynamics is used to reveal the mechanism of  $\text{Li}^+$  diffusion in  $\text{Li}_2\text{CO}_3$ . We first screen all of the possible point-defect energies in  $\text{Li}_2\text{CO}_3$ . We then demonstrate that the dominant defect within the voltage range of Li-ion batteries is excess interstitial  $\text{Li}^+$ . This is shown to diffuse by continuously displacing or *knocking-off*  $\text{Li}^+$  at a neighboring lattice site rather than by *direct-hopping* through empty spaces between  $\text{Li}_2\text{CO}_3$  lattice sites. The low-energy diffusion barrier of the knock-off mechanism is controlled by the coordination number with O anions rather than by the size of the open channels in the  $\text{Li}_2\text{CO}_3$  structure. We propose that this mechanism generally applies to ionic conductors with isolated polyhedral anions or layered tetrahedral networks. A numerical solution of a one-dimensional (1D) diffusion model based on the knock-off mechanism (inner layer) and pore diffusion (outer layer), with DFT-computed parameters, is then developed to predict the strongly coupled isotope concentration evolution observed in the Lu and Harris<sup>17</sup> experiments. Our two-layer/two-mechanism diffusion model is in accordance with the unusual isotope ratio  $^6\text{Li}^+/^7\text{Li}^+$  profile that increases from the SEI surface and peaks at a depth of 5 nm, where the main component of SEI becomes  $\text{Li}_2\text{CO}_3$ . In actual batteries, the SEI may in fact be quite complex, with substantial variation in composition and structure, as a result of different carbonates and lithium salts in nonaqueous electrolytes, electrode materials, charging/discharging mode, and temperature. Despite such complexities, the multiscale diffusion model presented herein, which is based upon insights acquired from DFT and is shown to be in close accord with isotope measurements in experiments,<sup>17</sup> can be readily adapted to model  $\text{Li}^+$  diffusion in substantially more complicated SEI films.

## 2. METHODS

**2.1. Density Functional Theory Calculations.** All first-principles calculations were conducted with the Vienna *Ab Initio* Simulation Package, a plane wave density functional code.<sup>22</sup> Potentials constructed by the projector-augmented wave method were used for the elements.<sup>23</sup> The exchange-correlation part of the density functional was treated within the local density approximation (LDA) of Ceperley and Alder<sup>24</sup> as parametrized by Perdew and Zunger.<sup>25</sup> Valence electron configurations for the elemental constituents are as follows: Li,  $1s^2 2s^1$ ; C,  $2s^2 2p^2$ ; and O,  $2s^2 2p^4$ . The cutoff energy for the plane-wave basis was 520 eV, and a  $2 \times 4 \times 3$  Monkhorst–Pack  $k$ -point mesh for the  $\text{Li}_2\text{CO}_3$  unit cell (24 atoms) was sufficient to converge the electronic energy to  $10^{-7}$  eV/unit cell. Hellman–Feynman force convergence was achieved at 0.01 eV/Å. In charged defects calculations, we controlled the total number of electrons in the supercell to compensate for excess charge from the defects. For example, one excess electron was added to the supercell for a negatively charged Li vacancy. A jellium background charge was used to neutralize supercells with charged defects.<sup>26</sup> Computed  $\text{Li}_2\text{CO}_3$  lattice parameters are within 2.5% of experimental values at 298 K.<sup>27</sup> Analyses of site-projected density of states and charge density difference contours show that C–O bonds are covalent and  $\text{Li}^+$  (refer to both lattice  $\text{Li}^+$  and excess interstitial  $\text{Li}^+$  as discussed below) ionically

bonded to O ions. The computed  $\text{Li}_2\text{CO}_3$  bandgap from LDA is 4.868 eV; no experimental bandgap data are presently available. Phonon spectra and related vibrational properties were computed with the supercell (direct) method to lattice dynamics.<sup>28</sup> Displacements of  $\pm 0.02$  Å were applied to nonequivalent atoms in  $2 \times 2 \times 2$   $\text{Li}_2\text{CO}_3$  supercells. We noted no negative elasticity tensor components and no imaginary frequencies in the computed vibrational spectra of  $\text{Li}_2\text{CO}_3$ , in contrast to the literature.<sup>29</sup> Hence, we find that  $\text{Li}_2\text{CO}_3$  is both mechanically and thermodynamically stable.<sup>18</sup> Transition-state structures and associated minimum energy pathways for excess interstitial  $\text{Li}^+$  diffusion in  $\text{Li}_2\text{CO}_3$  were computed with the CI-NEB method<sup>30</sup> using three images and two endpoint structures. Phonon calculations on the endpoint structures used in the CI-NEB calculations demonstrated that each is vibrationally stable, and the corresponding transition-state structures exhibit only one imaginary frequency in their vibrational spectra. Ancillary GGA calculations within the Perdew–Burke–Ernzerhof method<sup>31</sup> revealed no dependence of our major conclusions on the choice of exchange–correlation functional.

**2.2. Experiments.** Fresh SEI films were grown on a Cu substrate with a  $^7\text{LiClO}_4$  electrolyte following Lu and Harris.<sup>17</sup> Structure and chemistry were subsequently characterized with TEM, HRTEM, and XPS. The Cu foils covered by SEI films were rinsed with dimethyl carbonate (DMC) to remove the salt, dried in a glovebox, and immediately transferred to X-ray photoelectron spectroscopy (XPS) and TEM analyses. Sample exposure in air was minimized, and each sample was immediately analyzed by either TEM or XPS. The chemical depth profile of SEI films, relative to the SEI surface or the electrolyte/SEI interface, was measured with a Physical Electronics Quantera Scanning Microprobe (monochromated Al K $\alpha$  source, 1486.6 eV). A 3 kV Ar<sup>+</sup> source was employed for XPS sputtering, and the sputter rate for the XPS depth profile was calibrated by sputtering through a 100 nm  $\text{SiO}_2$  layer on Si standard sample. We note that this technique has a higher detection limit (0.1 at%) than SIMS (ppb). To prepare SEI films for TEM observations, small strips ( $\sim 0.2$  cm  $\times$  0.8 cm) of raw material were cut from the center of the Cu foil disk. These strips were vacuum-embedded in epoxy (Epofix, Struers, Denmark). After the epoxy was cured at room temperature for 24 h, the epoxy blocks were sliced with a microtome into electron-transparent thin sections with a thickness around 150 nm. The microtome was a Leica UC6 Ultra-microtome with a diamond knife. The thin sections were floated on the surface of DMC (anhydrous,  $\geq 99\%$ , Sigma-Aldrich, USA) and captured with 3 mm diameter 300-mesh lacy carbon coated Cu TEM grids. An aberration-corrected JEOL JEM-2100F microscope operated at 200 kV was used for the TEM study. We did note that the crystallite density was unaffected by the exposure duration of the TEM e-beam, suggesting that the beam does not create crystallites.

### 3. RESULTS AND DISCUSSION

**3.1. Thermodynamics of the Dominant Diffusion Carrier in Crystalline  $\text{Li}_2\text{CO}_3$ .** Monoclinic  $\text{Li}_2\text{CO}_3$  (C2/c, No. 15,  $Z = 4$ ) consists of planar covalently bonded  $\text{CO}_3^{2-}$  groups stacked in a zig-zag fashion along [001].<sup>27</sup> Figure 1 shows that the planar  $\text{CO}_3^{2-}$  groups are aligned along [010] and stack along [001], forming a building block parallel to the  $bc$  plane (i.e., (100), which is highlighted by the dotted region). Such blocks stand side-by-side along [100], while shifting half of the distance between planar  $\text{CO}_3^{2-}$  anions along [001]. The  $\text{Li}^+$  ions are located between these blocks, mainly within the  $bc$  plane. Each  $\text{Li}^+$  ion is near a  $\text{CO}_3^{2-}$  anion (within the same plane) and ionically bonds (indicated by 80% charge transfer from Li to O) to four  $\text{O}^{2-}$  ions (two within the same plane and two in the blocks above and below the plane). The thermodynamically stable  $\text{Li}_2\text{CO}_3$  in the SEI is an electronic insulator with a bandgap of 4.868 eV (from our LDA calculations).

The crystal structure of monoclinic  $\text{Li}_2\text{CO}_3$  contains open spaces (e.g., see site *I* in Figure 1) between the two parallel planar  $\text{CO}_3^{2-}$  groups. It has been proposed that these open spaces,

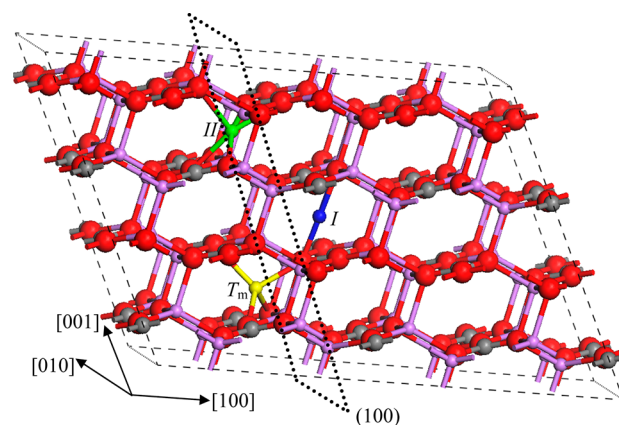


**Figure 1.** Monoclinic  $\text{Li}_2\text{CO}_3$  (C2/c, No. 15,  $Z = 4$ ) shown as a  $2 \times 2 \times 2$  supercell. Computed lattice parameters from LDA:  $a = 8.249$  Å,  $b = 4.906$  Å,  $c = 5.847$  Å,  $\alpha = \gamma = 90^\circ$ ,  $\beta = 114.553^\circ$  (each is within 2.5% of experimental values at 298 K<sup>27</sup>). Li, C, and O atoms at the lattice sites are represented by purple, gray, and red spheres, respectively. Blue, green, and yellow spheres show interstitial  $\text{Li}^+$  sites *I*, *II*, and  $T_m$ , with Li–O bonds highlighted. Interstitial site *II* lies within (100) which is denoted by the dotted black line.

which are part of the open channels along [010], provide diffusion pathways for interstitial  $\text{Li}^+$ .<sup>32</sup> The following hopping barriers have been provided from previous DFT calculations: 0.28 eV for an interstitial  $\text{Li}^+$  to diffuse through the open channel<sup>32</sup> and 0.23 eV for a neutral Li vacancy to hop along [001].<sup>33</sup> However, a more thorough approach, which we take here, is to first analyze the energetics of all of the possible point defects in monoclinic  $\text{Li}_2\text{CO}_3$ . Since the formation of an anion vacancy via removal of  $\text{CO}_3^{2-}$  or occupation of an interstitial site by  $\text{CO}_3^{2-}$  is energetically highly unfavorable, only  $\text{Li}^+$ -associated point defects (with different charge states) are considered. These are listed in Table 1.

**Table 1.**  $\text{Li}^+$ -Associated Point Defects (with Different Charge States) Computed in This Work

defect	definition
$V_{\text{Li}}$	neutral Li vacancy
$V_{\text{Li}}^-$	negatively charged Li vacancy
$\text{Li}_i$	neutral excess interstitial Li atom
$\text{Li}_i^+$	positively charged excess interstitial Li ion
$\text{Li}_{\text{FP}}$	neutral Li Frenkel pair
$\text{Li}_{\text{FP}}^+$	positively charged Li Frenkel pair
$\text{Li}_{\text{FP}}^-$	negatively charged Li Frenkel pair

A neutral or negatively charged Li vacancy is constructed by removing any one lattice Li atom or  $\text{Li}^+$  in the  $\text{Li}_2\text{CO}_3$   $2 \times 2 \times 2$  supercell, due to the crystallographic equivalency of all lattice Li sites. By searching for symmetry-unique sites at the center of empty spaces within the  $\text{Li}_2\text{CO}_3$  crystal structure, we identify the largest open space at a 4e site at the center of two planar  $\text{CO}_3^{2-}$ , noted as site *I* in Figure 1. The second largest open space is within the  $bc$  plane [highlighted as (100) by the dotted region in Figure 1] with the  $\text{Li}^+$  between the two  $\text{CO}_3^{2-}$  blocks at an 8f site which we label as site *II* in Figure 1. Another interstitial site,  $T_m$ , was selected to reproduce the results in the literature.<sup>32</sup> Intuitively, one would expect excess interstitial  $\text{Li}^+$  to locate at the open site *I* since the lattice Li, O and C atoms would appear to be less affected (maximum relaxation of 0.327 Å relative to lattice sites in perfect  $\text{Li}_2\text{CO}_3$ ) by  $\text{Li}^+$  at site *I*. However, by computing the



respective total energies of  $\text{Li}_2\text{CO}_3$  supercells with excess  $\text{Li}^+$  located at sites  $I$ ,  $II$ ,  $T_m$ , and four other identified interstitial sites (not shown in Figure 1), we found that the higher the coordination number of the excess interstitial  $\text{Li}^+$  with O ions, the lower the energy of the interstitial structure. The lowest total energy occurs when excess  $\text{Li}^+$  is at interstitial site  $II$ , where it forms five-fold Li–O bonds with bond lengths ranging from 1.956 to 2.024 Å (computed Li–O bond lengths in perfect  $\text{Li}_2\text{CO}_3$  fall within 1.849–1.950 Å). In contrast, site  $I$  has only two nearest-neighboring O ions, corresponding to a less favorable total energy that exceeds that of site  $II$  by 0.764 eV. Site  $T_m$  has four nearest-neighboring O ions and a higher total energy by 0.218 eV than that of site  $II$ . Four other identified interstitial sites follow a similar trend: their total energies are higher by 0.043–0.875 eV than that of site  $II$ , as the O ion coordination number goes from 4 to 2. Hence, from this point onward, excess interstitial  $\text{Li}^+$  refers to the energetically most favorable five-fold-coordinated site  $II$  in Figure 1. For the favored configuration of a Li Frenkel pair (an interstitial  $\text{Li}^+$  and a negatively charged vacancy), we find that the interstitial  $\text{Li}^+$  is also at site  $II$  and is about 3.681 or 5.166 Å from the vacancy within the same (100) plane. This interstitial can be an excess  $\text{Li}^+$  (off-stoichiometry but dilute) that may come from the electrolyte or the electrode, hereinafter denoted as  $\text{Li}_i^+$ .

During  $\text{Li}^+$  diffusion through an SEI film containing crystalline  $\text{Li}_2\text{CO}_3$ , both the chemical potentials of  $\text{Li}^+$  and the electron in the lithiated anode change during battery charging and discharging cycles. The chemical potentials of  $\text{Li}^+$  and electrons in  $\text{Li}_2\text{CO}_3$  are also related to the cell voltage. Therefore, the formation energy,  $E_f(i, q)$ , of a point defect  $i$  at charge state,  $q$ , in  $\text{Li}_2\text{CO}_3$  depends on the chemical potential of Li and the Fermi energy,  $\varepsilon_F$ , of the defect containing  $\text{Li}_2\text{CO}_3$ :<sup>34</sup>

$$E_f(i, q) = E_{\text{tot}}(i, q) - E_{\text{tot}}(\text{Li}_2\text{CO}_3, \text{bulk}) - n_{\text{Li}}\mu_{\text{Li}} + q(\varepsilon_F + E_V) \quad (1)$$

where  $E_{\text{tot}}(i, q)$  and  $E_{\text{tot}}(\text{Li}_2\text{CO}_3, \text{bulk})$  are the total energies of the  $\text{Li}_2\text{CO}_3$  supercell with and without a defect, respectively. The number of Li atoms (ions) added to ( $n_{\text{Li}} > 0$ ) or removed from ( $n_{\text{Li}} < 0$ ) the perfect supercell is  $n_{\text{Li}}$ , and  $\mu_{\text{Li}}$  is the chemical potential of Li. Note that  $\varepsilon_F$ , which is defined relative to the valence-band maximum ( $E_V$ ) of the perfect  $\text{Li}_2\text{CO}_3$ , changes with defect concentration. By assuming that all point defects exist at different concentrations (determined by their formation energy and temperature) in  $\text{Li}_2\text{CO}_3$ ,  $\varepsilon_F$  can be determined by requiring overall charge neutrality,<sup>35</sup> i.e.,

$$\sum_i q(i)N_s(i) \exp[-E_f(i, q)/k_B T] = N_C \exp[-(E_g - \varepsilon_F)/k_B T] - N_V \exp(-\varepsilon_F/k_B T) \quad (2)$$

Here,  $N_s(i)$  is the number of sites where defect  $i$  can be generated per unit volume,  $N_C$  ( $N_V$ ) is the integrated density of states (DOS) of the conduction (valence) band,  $E_g$  is the bandgap of a defect-free  $\text{Li}_2\text{CO}_3$ ,  $T$  is the temperature (300 K in our calculations), and  $k_B$  is Boltzmann's constant. Defect concentration,  $S(i, q)$ , can be computed directly from

$$S(i, q) = N_s(i) \exp[-E_f(i, q)/k_B T] \quad (3)$$

where  $E_f(i, q)$  is the computed formation energy from eqs 1 and 2. Note that  $\mu_{\text{Li}}$  is referenced to the bulk energy of Li metal, and it is thus related to the voltage in Li-ion batteries by setting the voltage of Li metal to be 0. Therefore,  $V = -(\mu_{\text{Li}} - \mu_{\text{Li}}^{\text{metal}}/e)$ , with  $V$  in volts and  $\mu_{\text{Li}}$  in eV. The range of chemical potential  $\mu_{\text{Li}}$

in eq 1 is not unlimited; on a negative electrode it should cover the entire intercalation process from SEI formation (0.8 V)<sup>36</sup> to Li metal formation (0 V). Figure 2a shows the  $E_f(i, q)$  computed

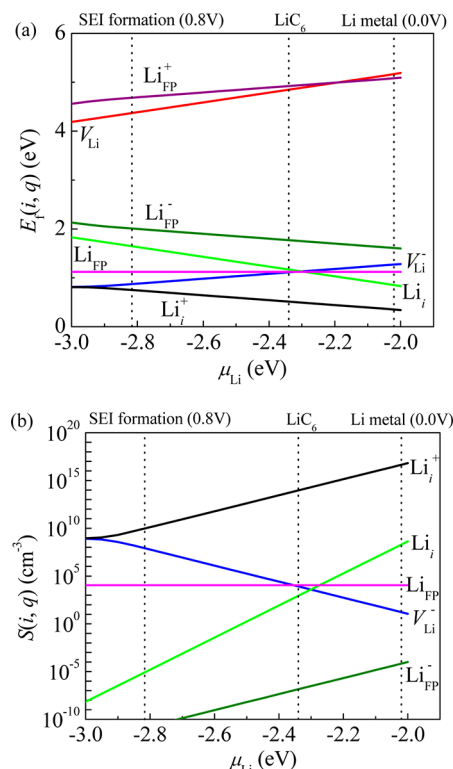


**Figure 2.** (a) Formation energies  $E_f(i, q)$  for all seven point defects in Table 1, and (b) defect concentrations  $S(i, q)$  for the five defects with the lowest  $E_f(i, q)$ . Both figures are calculated as a function of the chemical potential of Li,  $\mu_{\text{Li}}$ . The three vertical dotted lines correspond to  $\mu_{\text{Li}}$  for the formation of (from left to right) SEI,  $\text{LiC}_6$ , and Li metal. Within this chemical potential range,  $\text{Li}_i^+$  has the lowest formation energy and highest concentration, and thus is the main  $\text{Li}^+$  diffusion carrier.

according to eqs 1 and 2 at 300 K for all seven point defects in Table 1. Figure 2b shows the corresponding  $S(i, q)$  of the five defects with the lowest  $E_f(i, q)$  according to eq 3 in the range of chemical potential between SEI formation and Li metal. The chemical potential (cell voltage) for the formation of the fully intercalated graphite,  $\text{LiC}_6$ , is also calculated and highlighted as a vertical line at a computed value of  $\sim 0.3$  eV for reference. This is higher than the experimental value of  $\sim 0.1$  eV,<sup>37</sup> due to the overestimation of the Li–C binding in  $\text{LiC}_6$  with LDA.

Figure 2a shows that the formation energy for a positively charged excess interstitial Li ion,  $\text{Li}_i^+$ , is found to be the lowest ( $E_f = 0.74\text{--}0.34$  eV) among the seven defect types in Table 1. Consequently, Figure 2b shows that the concentration of  $\text{Li}_i^+$  is the highest relative to the concentrations of the other defects at equilibrium. As the formation energy of  $\text{Li}_i^+$  decreases with increasing  $\mu_{\text{Li}}$  (which corresponds to lowering the cell voltage), the concentration of  $\text{Li}_i^+$  increases from  $4.9 \times 10^9$  to  $2.3 \times 10^{16} \text{ cm}^{-3}$ . Christensen and Newman<sup>15</sup> modeled SEI growth assuming that a  $\text{Li}^+$  interstitial is the main defect in  $\text{Li}_2\text{CO}_3$  and its concentration is around  $6 \times 10^{18}$ – $3 \times 10^{19} \text{ cm}^{-3}$ . We note that their results are very close to the predicted  $\text{Li}_i^+$  concentration at low cell voltage in Figure 2b.

Our calculated formation energy of 1.121 eV for the neutral Frenkel pair ( $\text{Li}_{\text{FP}}$ ) does not change with  $\mu_{\text{Li}}$  and is in good agreement with the experimental value of 1.136 eV,<sup>18</sup> this supports our choice for the location of interstitial  $\text{Li}^+$  at site II in Figure 1. We note that  $E_{\text{f}} = 1.7$  eV (PW91-GGA) for the Frenkel pair reported in the literature<sup>32</sup> suggests that this is likely to be metastable since  $\text{Li}_i^+$  was presumed to occupy site  $T_{\text{m}}$  in Figure 1 instead of site II. Since  $\text{Li}_{\text{FP}}^+$  and  $V_{\text{Li}}$  have formation energies that exceed 4 eV, they are thermodynamically unstable in the range of cell voltages of Li-ion batteries, and their concentrations were therefore not included in Figure 2b. The formation energy of  $V_{\text{Li}}$  is comparable to those (PW91-GGA, 4.961 eV) of other Li ionic crystals reported in the literature, such as  $\text{Li}_2\text{O}$ .<sup>38</sup> Relative to the other charged defects in Table 1,  $V_{\text{Li}}$  is not a Li-ion diffusion carrier in either  $\text{Li}_2\text{CO}_3$  or  $\text{Li}_2\text{O}$ , in contrast to  $\text{Li}_i^+$ , which is expected to be the main diffusion carrier in both  $\text{Li}_2\text{CO}_3$  and  $\text{Li}_2\text{O}$  due to its ionic bonding<sup>38</sup> and the chemical potential range of Li.

According to Figure 2a,  $V_{\text{Li}}^-$  is the second most energetically preferred diffusion carrier in the cell voltage range. The formation energy for  $V_{\text{Li}}^-$ ,  $\text{Li}_{\text{p}}$  and  $\text{Li}_{\text{FP}}$  increases, decreases, and remains constant, respectively, with increasing  $\mu_{\text{Li}}$ . However, their energies cross at a cell voltage ranging from 0.2 to 0.3 V. If the cell voltage drops below this range, the secondary charge carrier becomes a neutral interstitial Li atom ( $\text{Li}_i$ ). If atomic Li indeed diffuses through  $\text{Li}_2\text{CO}_3$  into the electrolyte (even though the concentration of  $\text{Li}_i$  is smaller than  $\text{Li}_i^+$ ), then it could dissociate into one  $\text{Li}^+$  and one electron. This may be one of the mechanisms that explains electron leakage through the SEI film into the electrolyte,<sup>39</sup> resulting in self-discharging of a lithiated anode and/or SEI growth. This will be clarified further in the future.

**3.2. Knock-Off Diffusion Mechanism in Crystalline  $\text{Li}_2\text{CO}_3$ .** An interstitial atom can diffuse through lattice interstices without displacing lattice atoms via a direct-hopping or “interstitial mechanism”; this is the mechanism behind the hardening of tool steels, for example.<sup>40</sup> Alternatively, an interstitial atom can also diffuse into a host lattice site by displacing a neighboring lattice atom into an adjacent interstitial site via a knock-off or “interstitialcy mechanism.” This diffusion mechanism is proposed in some ionic crystals such as  $\text{AgCl}$ ,  $\text{CaF}_2$ , and doped  $\text{Si}$ .<sup>40,41</sup> In section 3.1, we provided theoretical evidence that the diffusion carrier in  $\text{Li}_2\text{CO}_3$  is an interstitial  $\text{Li}^+$  rather than a vacancy; however, the  $\text{Li}_i^+$  diffusion mechanism through  $\text{Li}_2\text{CO}_3$  remains to be determined. Here, we present a detailed comparison of the direct-hopping and the knock-off diffusion mechanisms.

Diffusion of  $\text{Li}_i^+$  is highly anisotropic due to the complex  $\text{Li}_2\text{CO}_3$  crystal structure. There are many interstitial sites in  $\text{Li}_2\text{CO}_3$  that are crystallographically equivalent to site II to which a  $\text{Li}_i^+$  can diffuse. However, we find from CI-NEB calculations that the energy barriers for diffusion into these other sites are typically quite high. For example, penetrating the covalently bonded  $\text{CO}_3^{2-}$  anion to hop directly along  $[101]$ ,  $[10\bar{1}]$ ,  $[\bar{1}01]$ , or  $[\bar{1}0\bar{1}]$  (see Figure 1) is forbidden. Alternatively, hopping along  $[100]$  means that  $\text{Li}_i^+$  must pass through the open channel (site I in Figure 1) between two  $\text{CO}_3^{2-}$ , where the  $\text{Li}_i^+$  energy is higher by 0.764 eV compared with site II in Figure 1. There are four neighboring (equivalent) interstitial  $\text{Li}_i^+$  sites (not shown in Figure 1) around site II along four ( $[01\bar{1}]$ ,  $[011]$ ,  $[0\bar{1}1]$ , and  $[01\bar{1}]$ ) directions within the (100) plane, because all  $\text{Li}_i^+$  ions are situated around this plane. The upper right inset in Figure 3(a) shows a portion of a  $2\times 2\times 2$   $\text{Li}_2\text{CO}_3$  supercell with a  $\text{Li}_i^+$  diffusion

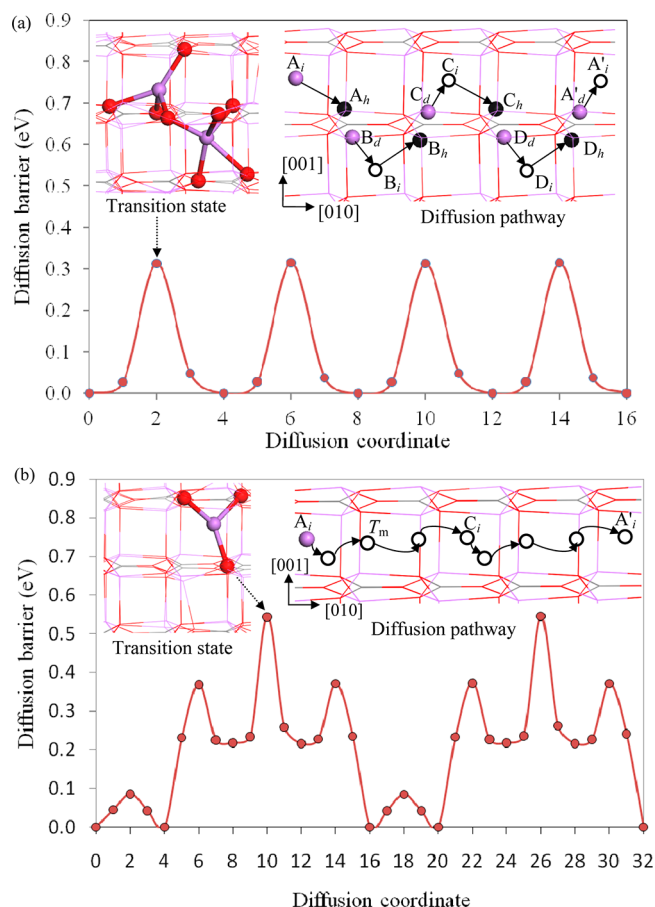


**Figure 3.** Energy profile, transition-state structure (upper left inset), and schematic diagram of diffusion pathway (upper right inset) of the  $\text{Li}_i^+$  diffusion from site  $A_i$  along  $[010]$  direction following the (a) knock-off and (b) direct-hopping mechanisms. In all the atomic structures, the lines sketch the perfect  $\text{Li}_2\text{CO}_3$  crystalline structure projected along the  $[100]$  direction or a direct view of the dotted (100) plane in Figure 1.  $A_i$  is the initial location of the diffusing  $\text{Li}_i^+$ , which is the same location as site II in Figure 1.  $A'_i$  is the periodic image of  $A_i$ , and the metastable interstitial site  $T_{\text{m}}$  is the same  $T_{\text{m}}$  shown in Figure 1. In the schematic diagrams of the diffusion pathways [upper right insets in (a) and (b)], black and hollow spheres mark sites through which  $\text{Li}_i^+$  diffuses. Subscripts  $i$ ,  $d$ , and  $h$  refer to interstitial, distorted lattice, and nondistorted lattice sites, respectively. In (a), the initial positions of  $A$ ,  $B$ ,  $C$ ,  $D$ , and  $A'$  (periodic image of  $A$ ) are highlighted in purple spheres. These atoms take turns as the diffusing interstitials and move in four knock-off steps: (1)  $A_i \rightarrow A_{ih}$ ,  $B_d \rightarrow B_i$ ; (2)  $B_i \rightarrow B_{dh}$ ,  $C_d \rightarrow C_i$ ; (3)  $C_i \rightarrow C_{dh}$ ,  $D_d \rightarrow D_i$ ; (4)  $D_i \rightarrow D_{dh}$ ,  $A'_d \rightarrow A'_i$ . The endpoint structures after each knock-off step correspond to diffusion coordinates of 4, 8, 12, and 16 in the computed diffusion energy profile. In (b), the  $\text{Li}_i^+$  at site  $A_i$  diffuses through the hollow spheres (starting from the left), representing the locations of most stable and metastable interstitial sites. These correspond to diffusion coordinates of 4, 8, 12, 16, 20, 24, 28, and 32 in the computed diffusion energy profile. The transition-state structures (upper left inset figure) correspond to diffusion coordinates 2 for (a) and 10 for (b). The two purple spheres in the transition state in (a) are due to the simultaneous diffusion steps of  $A_i \rightarrow A_{ih}$  and  $B_d \rightarrow B_i$ . In the transition-state structure of (a), the diffusing  $\text{Li}_i^+$  (purple) is five-fold coordinated with O (red), whereas it is three-fold coordinated in the transition structure of (b).

pathway. Black and hollow spheres mark sites through which  $\text{Li}_i^+$  passes during diffusion. Subscripts  $i$ ,  $d$ , and  $h$  refer to interstitial, distorted lattice, and nondistorted lattice sites, respectively. Their relationship can be understood as follows. The occurrence of  $\text{Li}_i^+$

at an interstitial site  $A_i$  causes  $\text{Li}^+$  at nondistorted lattice site  $A_h$  to relax to the distorted lattice site  $B_d$ . We consider two possibilities for continued  $\text{Li}_i^+$  diffusion. The first is direct hopping of  $\text{Li}_i^+$  from site  $A_i$  (equivalent to site  $II$  in Figure 1) to  $B_i$  along  $[01\bar{1}]$ . The barrier computed from CI-NEB for this process is as high as  $\sim 10$  eV, since  $\text{Li}_i^+$  must come within  $0.862 \text{ \AA}$  (which is one-half of the typical Li–O bond length) of an  $\text{O}^{2-}$  ion. The second possibility for  $\text{Li}_i^+$  diffusion following the evacuation of site  $B_d$  and the occupation of site  $A_h$  (due to the occurrence of  $\text{Li}_i^+$  at site  $B_i$ ) is a cooperative diffusion process along  $[01\bar{1}]$ , that is,  $A_i \rightarrow A_h$ ,  $B_d \rightarrow B_i$ . In other words, a  $\text{Li}_i^+$  at site  $A_i$  diffuses along  $[01\bar{1}]$  to a nondistorted lattice site  $A_h$  and simultaneously knocks-off an existing  $\text{Li}^+$  at the distorted lattice site  $B_d$  to the interstitial site  $B_i$ . This knock-off process has a net 0.31 eV energy barrier. The computed energy barrier for this cooperative diffusion of  $\text{Li}_i^+$  at  $A_i$  with  $\text{Li}^+$  at  $B_d$  from CI-NEB is substantially lower than that for the direct-hopping mechanism.

There are in fact four neighboring lattice  $\text{Li}^+$  ions, similar to that at  $A_h$  in the upper right inset in Figure 3a, in the range of  $2.417\text{--}2.647 \text{ \AA}$  from a  $\text{Li}_i^+$  ion within the highlighted (100) plane in Figure 1. Thus,  $\text{Li}_i^+$  can knock-off any of the four neighboring lattice  $\text{Li}^+$  with nearly equivalent probabilities, to effectively achieve a diffusion step along  $[01\bar{1}]$ ,  $[011]$ ,  $[0\bar{1}1]$ , or  $[0\bar{1}\bar{1}]$ . The net effect of these knock-off steps along four directions is macroscopic diffusion of the  $\text{Li}_i^+$  within the (100) plane in  $\text{Li}_2\text{CO}_3$ . For example, the upper right inset in Figure 3a shows one possible step beyond  $B_i \rightarrow B_h$ ,  $C_d \rightarrow C_i$ . Here, a  $\text{Li}_i^+$  at interstitial site  $B_i$  diffuses along  $[011]$  to a nondistorted lattice site  $B_h$  and simultaneously knocks-off an existing  $\text{Li}^+$  at the distorted lattice site  $C_d$  to the new interstitial site  $C_i$ . After  $A_i \rightarrow A_h$ ,  $B_d \rightarrow B_i$  and  $B_i \rightarrow B_h$ ,  $C_d \rightarrow C_i$ , the  $\text{Li}_i^+$  at site  $A_i$  has effectively diffused through a full lattice length ( $4.906 \text{ \AA}$ ) along  $[010]$  to  $C_i$ . In each step, the distances traveled by the  $\text{Li}^+$  ions involved in knock-off are all within  $1.860\text{--}2.043 \text{ \AA}$ . The sum of these distances from the three  $\text{Li}^+$  ions involved in the two “knock-off” steps is only  $4.086 \text{ \AA}$ , which is shorter than the full lattice length of  $4.906 \text{ \AA}$ . Thus, the total travel distance of  $A_i \rightarrow A_h$ ,  $B_d \rightarrow B_i$  and  $B_i \rightarrow B_h$ ,  $C_d \rightarrow C_i$  is shorter than that of a straight line from  $A_i$  to  $C_i$ . After another two similar knock-off steps,  $C_i \rightarrow C_h$ ,  $D_d \rightarrow D_i$  then  $D_i \rightarrow D_h$ ,  $A'_d \rightarrow A'_i$ , the  $\text{Li}^+$  ion at the distorted lattice site  $A'_d$  is knocked-off by  $\text{Li}_i^+$  at site  $D_i$  and becomes the periodic image of  $\text{Li}_i^+$  at (the initial) site  $A_i$  in the original structure. As shown in the computed diffusion barrier profile in Figure 3a, wherein  $A_i$  corresponds to diffusion coordinate 0, the barrier height for each knock-off step is  $\sim 0.31$  eV. Therefore, the  $\text{Li}_i^+$  diffuses along  $[010]$  with a diffusion energy barrier of  $E_m \approx 0.31$  eV. The transition-state configuration is shown in the upper left inset of Figure 3a.

For comparison with results from the knock-off mechanism, direct-hopping of  $\text{Li}_i^+$  along  $[010]$  is considered in Figure 3b. Perhaps the most intuitively appealing diffusion mechanism for  $\text{Li}_i^+$ ,<sup>32</sup> direct-hopping follows a pathway through the open channels formed between two planar  $\text{CO}_3^{2-}$  (also see Figure 1). Our proposed  $\text{Li}_i^+$  hopping pathway is shown in the upper right inset in Figure 3b. As in the knock-off pathway in Figure 3a,  $A_i$  is set as the initial site of the diffusing  $\text{Li}_i^+$  and corresponds to diffusion coordinate 0 in the diffusion barrier profile. The hopping pathway shown in the upper right inset in Figure 3b is not a straight line along  $[010]$ ; rather, it is a nonlinear path that passes through many interstitial sites in  $\text{Li}_2\text{CO}_3$ . The hollow spheres (starting from the left in the upper right inset in Figure 3b) represent the locations of the interstitial (i.e., initially unoccupied) sites corresponding to diffusion coordinates 4, 8, 12, 16, 20, 24, 28,

and 32, respectively, in the diffusion barrier profile in Figure 3b. Coordinates 16 and 32 correspond to the periodic translations of  $A_i$  along  $[010]$ . Coordinates 4 and 20 correspond to additional interstitial structures that are energetically equivalent to coordination 0. Coordinates 8 (site  $T_m$  in Figure 1),<sup>42</sup> 12, 24, and 28 are energetically equivalent metastable interstitial structures. These structures (i.e., those with the greatest stability and those that are metastable) form the end points for the eight transition-state searches used to compute the diffusion barrier profile in Figure 3b. The transition state between coordinates 8 and 12, which is shown in the upper left inset of Figure 3b, occurs at 0.54 eV relative to the most stable interstitial structure at  $A_i$ . This barrier, which is the highest of all diffusion barriers from CI-NEB, is nearly twice the 0.31 eV barrier computed for the knock-off mechanism in Figure 3a. In the direct-hopping mechanism, diffusion of a full lattice length ( $A_i \rightarrow C_i$ ,  $4.906 \text{ \AA}$ ) along  $[010]$  requires that  $\text{Li}_i^+$  must move  $7.496 \text{ \AA}$ , which is nearly twice that required by the knock-off mechanism ( $4.086 \text{ \AA}$ ). Therefore, not only does the knock-off mechanism have a lower diffusion barrier compared with the direct-hopping mechanism in one knock-off step (e.g.,  $A_i \rightarrow A_h$ ,  $B_d \rightarrow B_i$  in Figure 3a) along  $[01\bar{1}]$ ,  $[011]$ ,  $[0\bar{1}1]$ , or  $[0\bar{1}\bar{1}]$ , but the barrier is also lower along other macroscopic diffusion directions, such as  $[010]$ ,  $[001]$ ,  $[011]$ , or  $[0\bar{1}\bar{1}]$  (within the (100) plane), along which the knock-off mechanism can also proceed. This further demonstrates that diffusion of  $\text{Li}_i^+$  in  $\text{Li}_2\text{CO}_3$  is highly anisotropic; i.e. it is easier within a (100) plane, but harder along  $[100]$ .

The self-diffusion coefficient for the  $\text{Li}_i^+$  in  $\text{Li}_2\text{CO}_3$  can be computed with  $D = \frac{1}{2} v^* (\Delta x)^2 \exp(-E_m/k_B T)$ , where  $E_m = 0.31$  eV for the knock-off mechanism and  $E_m = 0.54$  eV for direct-hopping mechanism,  $v^*$  is the lattice vibrational frequency ( $\sim 10^{13}$  Hz estimated from our phonon calculations),  $\Delta x$  is the distance for each migration step ( $4.906 \text{ \AA}$  for both mechanisms),  $T$  is the temperature (300 K in our calculations), and  $k_B$  is Boltzmann's constant. We find  $D = 1.1 \times 10^{-7} \text{ cm}^2/\text{s}$  for the knock-off mechanism and  $8.4 \times 10^{-12} \text{ cm}^2/\text{s}$  for the direct-hopping mechanism.

Given that the concentration of  $\text{Li}_i^+$  in  $\text{Li}_2\text{CO}_3$  is dilute, the flux of  $\text{Li}_i^+$  can move through diffusion and migration via  $N_{\text{Li}} = -D(\partial c_{\text{Li}}/\partial x) - (F/RT)Dc_{\text{Li}}(\partial \Phi/\partial x)$ , where  $D$  is the diffusion coefficient of  $\text{Li}_i^+$ ,  $c_{\text{Li}}$  is the concentration of  $\text{Li}_i^+$ ,  $F$  is Faraday's constant,  $R$  is the gas constant,  $T$  is the temperature,  $x$  is the spatial coordination through the SEI film, and  $\Phi$  is the electric potential. Both  $D$  and  $c_{\text{Li}}$  (Figure 2b) have been directly computed from DFT calculations. In their  $\text{Li}_2\text{CO}_3$ –SEI model, Christensen and Newman<sup>15</sup> used  $D \approx 10^{-9}\text{--}10^{-10} \text{ cm}^2/\text{s}$ , which results in a predicted SEI film resistance that is several orders of magnitude higher than typical experimental values estimated from impedance measurements ( $\sim 1800\text{--}10000 \Omega \cdot \text{cm}^2$ ).<sup>43</sup> They concluded that  $\text{Li}_i^+$  transport in  $\text{Li}_2\text{CO}_3$  must follow pathways along grain boundaries. However, our computed  $D$  for the knock-off mechanism along the (100) plane is 2–3 orders of magnitude higher than their values and predicts an ionic resistance of  $6000 \Omega \cdot \text{cm}^2$  for a 20 nm thick SEI film, consistent with experiments.<sup>43</sup> This suggests that the fastest diffusion in bulk  $\text{Li}_2\text{CO}_3$  provided by the knock-off mechanism can be of the same order as grain boundary diffusion. Because the ionic conductivity of  $\text{Li}_2\text{CO}_3$  due to  $\text{Li}_i^+$  migration under the electrical potential gradient is proportional to  $Dc_{\text{Li}}$ , the activation energy barrier for the conductivity includes both the formation energy of  $\text{Li}_i^+$  and its diffusion barrier. The activation energy barrier in  $\text{Li}_2\text{CO}_3$  is therefore  $E_f + E_m \approx 0.7$  eV at low voltage, in reasonable accord with the 0.6 eV value from electrochemical impedance



spectroscopy.<sup>44–46</sup> But in addition to temperature, we point out here that the voltage also changes the formation energy of  $\text{Li}_i^+$  (as shown in Figure 2a) between 0 and 0.8 V. The activation energy barrier will be in the 0.67–1.07 eV range for the knock-off mechanism and between the 0.92–1.32 eV range for the direct-hopping mechanism in the same voltage range. Thus, the computed activation energy barrier range for the knock-off mechanism compares much more favorably with experiments than does the range computed for the direct-hopping mechanism.

It is the Li–O bond coordination associated with the interstitial in the knock-off diffusion pathway that renders it the energetically preferred diffusion mechanism over the direct-hopping mechanism. Clearly,  $\text{Li}_i^+$  maintains a higher coordination number with O ions in the knock-off mechanism. The  $\text{Li}_i^+$  at the interstitial site (site II in Figure 1 and  $A_i$  in Figure 3) has five-fold Li–O bonds, as we have shown in Figure 1. In the transition state for the knock-off mechanism (upper left inset in Figure 3a), the diffusing  $\text{Li}_i^+$  (e.g., coming from site  $A_i$ ) coordinates with four O ions (Li–O bond lengths are 1.854, 1.882, 1.897, and 2.073 Å, respectively), while the  $\text{Li}^+$  being knocked-off (e.g., coming from site  $B_d$ ) has five-fold Li–O coordination (bond lengths are 1.898, 1.919, 1.968, 2.136, and 2.153 Å, respectively). In comparison, the transition state computed for the direct-hopping mechanism in Figure 3b has a low Li–O coordination number for the diffusing  $\text{Li}_i^+$  (three Li–O bonds of lengths 1.764, 1.774, and 1.899 Å), which corresponds to the net 0.54 eV diffusion energy barrier. This is consistent with our observation that the higher coordination between Li and O ions leads to a lower total energy. This is revealed by our analysis in section 3.1 of the total energies of  $\text{Li}_2\text{CO}_3$  supercells with excess  $\text{Li}^+$  located at various interstitial sites. It is the formation of five-fold Li–O bonds that lowers the diffusion energy barriers associated with the knock-off mechanism relative to direct-hopping mechanism in  $\text{Li}_2\text{CO}_3$ .

Seitz<sup>47</sup> first discussed the “interstitialcy” or knock-off mechanism without referring to any specific material; the interstitial atom was assumed to diffuse to the lattice site of the atom it knocks-off. However, we observe that in  $\text{Li}_2\text{CO}_3$ , the lattice site (e.g.,  $A_h$ ) at which  $\text{Li}_i^+$  arrives, and that (e.g.,  $B_d$ ) from which the lattice  $\text{Li}^+$  diffuses, are separated from each other by  $\sim 0.3$ – $1.0$  Å. This is because of the complicated arrangement of  $\text{CO}_3^{2-}$ , the long-range ( $\sim 1.088$  Å) structural distortion that the  $\text{Li}_i^+$  causes, and the fact that  $\text{Li}_i^+$  tends to coordinate with more O ions during diffusion. The basic idea for the interstitial diffusion mechanism was two-fold: (1) Although there are relatively large open channels along certain directions, the incorporated interstitial ion prefers to stay close to each side of a given channel (e.g., site II in Figure 1) to maintain a high cation–anion coordination number with the neighboring counterions (i.e., neighboring, oppositely charged ions around the diffusing ion), causing highly anisotropic diffusion (along the (100) plane in this case). (2) Not only is the coordination number for the interstitial  $\text{Li}^+$  higher than that for a lattice ion, but maintaining higher cation–anion coordination numbers during diffusion results in a lower diffusion energy barrier. This latter case is the fundamental reason that diffusion in  $\text{Li}_2\text{CO}_3$  is energetically predisposed to the knock-off mechanism. Actually, the knock-off diffusion mechanism is quite general for other ionic structures and has been observed in compounds with isolated polyhedral anions or layered tetrahedral networks such as  $\text{LiBO}_2$ ,<sup>48</sup>  $\text{Li}_2\text{SO}_4$ ,<sup>49</sup>  $\text{Li}_3\text{PO}_4$ ,<sup>50</sup>  $\text{Li}_4\text{SiO}_4$ ,<sup>51</sup>  $\text{LiF}$ , and  $\text{Li}_2\text{O}$ ,<sup>52</sup> as proposed on the basis of DFT results while lacking experimental confirmation.

**3.3. Computed Lithium Concentration Profiles in  $\text{Li}_2\text{CO}_3$ .** Tracer diffusion measurement is one way to differentiate the

knock-off vs the direct-hopping mechanisms.<sup>17,53</sup> To explain the isotope ratio  ${}^6\text{Li}^+ / {}^7\text{Li}^+$  profiles measured by Lu and Harris’s measurement,<sup>17</sup> we formulate a 1D lattice diffusion model following King’s approach.<sup>54</sup>

We consider a thin layer of  $\text{Li}_2\text{CO}_3$  on a substrate (Cu) that cannot be lithiated. This thin  $\text{Li}_2\text{CO}_3$  layer consists of alternating lattice and interstitial (010) planes, as illustrated in Figure 4,

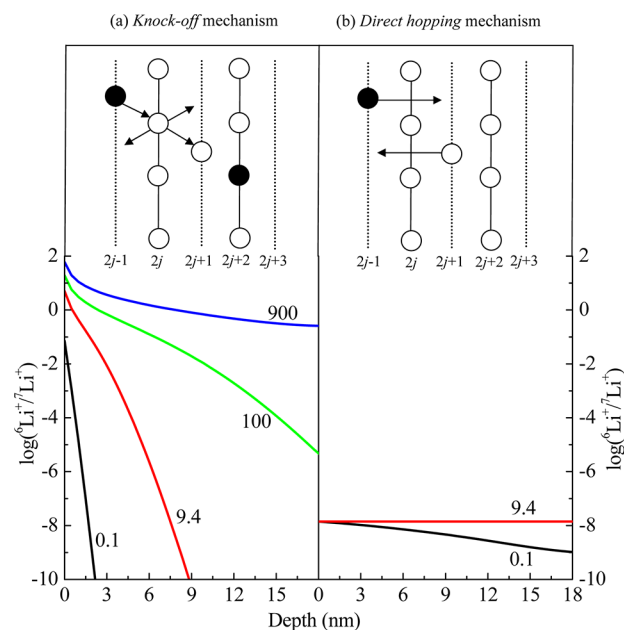


**Figure 4.** Time (unit: seconds) evolution of the depth profile of the log of the ( ${}^6\text{Li}^+ / {}^7\text{Li}^+$ ) with the (a) knock-off and (b) direct-hopping mechanisms. Insets are schematic drawings of two mechanisms. The atomic (010) planes noted by dotted lines are for interstitial sites and the solid lines are for lattices sites. Horizontal distance between two adjacent dotted (or solid) lines is 4.906 Å (i.e., distance for each migration step). Open symbols represent  ${}^7\text{Li}^+$ , and solid symbols represent  ${}^6\text{Li}^+$ .

labeled with even and odd numbers, respectively. By ignoring crystal imperfections and vacancies in the crystalline lattice, the two isotopes, whose respective concentrations on the  $2j$ th lattice plane are  ${}^6\text{Li}_{2j}^L(t)$  and  ${}^7\text{Li}_{2j}^L(t)$ , will occupy all the lattice sites on the  $2j$ th lattice plane so that  ${}^6\text{Li}_{2j}^L(t) + {}^7\text{Li}_{2j}^L(t) = N_s^L$ , where  $N_s^L$  is the density of lattice sites (superscript “L” refers to the lattice site). Note that, for simplicity, the interstitial sites  $N_s^I$  and interstitial concentration  $S(i,q)$  in eq 3 for the defect  $\text{Li}_i^+$  are denoted as  $N_s^I$  and  $S^I$  in section 3.3 (superscript “I” refers to the interstitial site).

On the  $2j+1$ th interstitial plane, the concentrations of two isotopes,  ${}^6\text{Li}_{2j+1}^I(t)$  and  ${}^7\text{Li}_{2j+1}^I(t)$ , add up to the interstitial concentration, as  ${}^6\text{Li}_{2j+1}^I(t) + {}^7\text{Li}_{2j+1}^I(t) = S^I$ ; the rest of the interstitial sites, which are empty, are referred to as  $V_{2j+1}^I(t)$  and  $V_{2j+1}^I(t) = N_s^I - {}^6\text{Li}_{2j+1}^I(t) - {}^7\text{Li}_{2j+1}^I(t)$ . Based on the crystal structure of  $\text{Li}_2\text{CO}_3$ ,  $N_s^L$  and  $N_s^I$  are the same and equal to  $3.72 \times 10^{22} \text{ cm}^{-3}$ . The interstitial concentration,  $S^I$ , is set to be  $5.2 \times 10^{14} \text{ cm}^{-3}$  [derived from  $E_f(i,q) = 0.467$  eV at a cell voltage of 0.2 V].

In the direct-hopping mechanism, the interstitial  ${}^7\text{Li}^+$  or  ${}^6\text{Li}^+$  directly hops to the next interstitial layer along [010] as shown by the arrow in Figure 4b. Therefore, the change of concentration of interstitial  $\text{Li}^+$  on the  $2j+1$ th interstitial plane,  ${}^6\text{Li}_{2j+1}^I(t)$  (or  ${}^7\text{Li}_{2j+1}^I(t)$ ), over time is determined from



$$\frac{d^6\text{Li}_{2j+1}^I}{dt} = \frac{1}{2} \nu^* \exp(-E_m/k_B T) ({}^6\text{Li}_{2j-1}^I - 2{}^6\text{Li}_{2j+1}^I + {}^6\text{Li}_{2j+3}^I) \quad (4)$$

where  $E_m$  is the interstitial direct-hopping energy barrier (0.54 eV),  $T$  is temperature (300 K in our calculations), and  $k_B$  is Boltzmann's constant. Note that  ${}^7\text{Li}^+$  at the lattice sites do not participate in diffusion in direct-hopping. However, in the knock-off mechanism in Figure 4a, the concentrations of  $\text{Li}^+$  at lattice sites,  ${}^6\text{Li}_{2j}^L(t)$  and  ${}^7\text{Li}_{2j}^L(t)$ , are coupled with the concentrations of interstitial  $\text{Li}^+$ , i.e.,  ${}^6\text{Li}_{2j\pm 1}^I(t)$  and  ${}^7\text{Li}_{2j\pm 1}^I(t)$ . The probability of a forward knock-off step, described in section 3.2, is determined by the concentration of  ${}^6\text{Li}^+$  on the  $2j-1$ th interstitial plane, denoted by  ${}^6\text{Li}_{2j-1}^I$ , the concentration of  ${}^7\text{Li}^+$  on the  $2j$ th lattice plane, denoted by  ${}^7\text{Li}_{2j}^L$ , and the vacancy concentration on the  $2j+1$ th interstitial plane,  $V_{2j+1}^I$ . Including all four possible knock-off diffusion steps along  $[01\bar{1}]$ ,  $[011]$ ,  $[\bar{0}11]$ , or  $[0\bar{1}1]$ , the evolution of the isotope concentrations  ${}^6\text{Li}_{2j}^L(t)$ ,  ${}^6\text{Li}_{2j+1}^L(t)$ , and  ${}^7\text{Li}_{2j+1}^L(t)$  can be computed from the following diffusion equations:

$$\begin{aligned} \frac{d^6\text{Li}_{2j}^L}{dt} = & \frac{\nu^* \exp(-E_m/k_B T)}{4(N_s^L)^2} \times \\ & [{}^7\text{Li}_{2j}^L ({}^6\text{Li}_{2j-1}^I V_{2j+1}^I + {}^6\text{Li}_{2j+1}^I V_{2j-1}^I) \\ & + {}^7\text{Li}_{2j}^L ({}^6\text{Li}_{2j-1}^I V_{2j-1}^I + {}^6\text{Li}_{2j+1}^I V_{2j+1}^I) \\ & - {}^6\text{Li}_{2j}^L ({}^7\text{Li}_{2j-1}^I V_{2j+1}^I + {}^7\text{Li}_{2j+1}^I V_{2j-1}^I) \\ & - {}^6\text{Li}_{2j}^L ({}^7\text{Li}_{2j-1}^I V_{2j-1}^I + {}^7\text{Li}_{2j+1}^I V_{2j+1}^I)] \end{aligned} \quad (5)$$

$$\begin{aligned} \frac{d^6\text{Li}_{2j+1}^I}{dt} = & \frac{\nu^* \exp(-E_m/k_B T)}{4(N_s^L)^2} \times \\ & [V_{2j+1}^I ({}^7\text{Li}_{2j-1}^I {}^6\text{Li}_{2j}^L + {}^7\text{Li}_{2j+3}^I {}^6\text{Li}_{2j+2}^L) \\ & + V_{2j+1}^I ({}^6\text{Li}_{2j-1}^I {}^6\text{Li}_{2j}^L + {}^6\text{Li}_{2j+3}^I {}^6\text{Li}_{2j+2}^L) \\ & + V_{2j+1}^I {}^7\text{Li}_{2j+1}^I ({}^6\text{Li}_{2j}^L + {}^6\text{Li}_{2j+2}^L) \\ & - {}^6\text{Li}_{2j+1}^I (V_{2j-1}^I {}^7\text{Li}_{2j}^L + V_{2j+3}^I {}^7\text{Li}_{2j+2}^L) \\ & - {}^6\text{Li}_{2j+1}^I (V_{2j-1}^I {}^6\text{Li}_{2j}^L + V_{2j+3}^I {}^6\text{Li}_{2j+2}^L) \\ & - V_{2j+1}^I {}^6\text{Li}_{2j+1}^I ({}^7\text{Li}_{2j}^L + {}^7\text{Li}_{2j+2}^L)] \end{aligned} \quad (6)$$

$$\begin{aligned} \frac{d^7\text{Li}_{2j+1}^I}{dt} = & \frac{\nu^* \exp(-E_m/k_B T)}{4(N_s^L)^2} \times \\ & [V_{2j+1}^I ({}^6\text{Li}_{2j-1}^I {}^7\text{Li}_{2j}^L + {}^6\text{Li}_{2j+3}^I {}^7\text{Li}_{2j+2}^L) \\ & + V_{2j+1}^I ({}^7\text{Li}_{2j-1}^I {}^7\text{Li}_{2j}^L + {}^7\text{Li}_{2j+3}^I {}^7\text{Li}_{2j+2}^L) \\ & + V_{2j+1}^I {}^6\text{Li}_{2j+1}^I ({}^7\text{Li}_{2j}^L + {}^7\text{Li}_{2j+2}^L) \\ & - {}^7\text{Li}_{2j+1}^I (V_{2j-1}^I {}^6\text{Li}_{2j}^L + V_{2j+3}^I {}^6\text{Li}_{2j+2}^L) \\ & - {}^7\text{Li}_{2j+1}^I (V_{2j-1}^I {}^7\text{Li}_{2j}^L + V_{2j+3}^I {}^7\text{Li}_{2j+2}^L) \\ & - V_{2j+1}^I {}^7\text{Li}_{2j+1}^I ({}^6\text{Li}_{2j}^L + {}^6\text{Li}_{2j+2}^L)] \end{aligned} \quad (7)$$

where  $E_m$  is the diffusion energy barrier (0.31 eV from CI-NEB calculations) in the knock-off mechanism. The diffusion equations for the direct-hopping mechanism can be solved analytically. However, the strong coupling in the diffusion equations for the knock-off mechanism requires that they be numerically

solved. We therefore solve the diffusion equations for both mechanisms numerically with the same initial and boundary conditions.

We assume that the  $\text{Li}_2\text{CO}_3$  initially contains a constant  ${}^7\text{Li}^+$  concentration equal to  $S^I$  at  $t = 0$  with no  ${}^6\text{Li}^+$ :

$$\begin{aligned} {}^7\text{Li}_{2j+1}^I(0) &= S^I = 5.241 \times 10^{14} \text{ cm}^{-3}, \\ {}^6\text{Li}_{2j+1}^I(0) &= 0, {}^6\text{Li}_{2j}^L(0) = 0, \\ j &= 1, 2, 3, \dots, 40 \end{aligned} \quad (8)$$

where  $j = 40$  corresponds to 40 lattice layers or a  $\sim 20$  nm thickness of the  $\text{Li}_2\text{CO}_3$  layer. During an isotope exchange experiment, we assume that all of the interstitial sites at the electrolyte/ $\text{Li}_2\text{CO}_3$  interface are replaced by  ${}^6\text{Li}^+$ , and the  ${}^6\text{Li}^+$  concentration at this interface is thereafter fixed. Since the soaking electrolyte has no  ${}^7\text{Li}^+$ , we assume that the  ${}^7\text{Li}^+$  concentration at the electrolyte/ $\text{Li}_2\text{CO}_3$  interface is zero. We also assume that any amount of  ${}^7\text{Li}^+$  that diffuses out of the  $\text{Li}_2\text{CO}_3$  into the electrolyte does not disturb the  ${}^7\text{Li}^+$  concentration at the electrolyte/ $\text{Li}_2\text{CO}_3$  interface due to the large volume of electrolyte. Thus, we impose a constant  ${}^6\text{Li}^+$  concentration at  $j = 0$  for all time with no  ${}^7\text{Li}^+$ :

$${}^6\text{Li}_1^I(t) = 5.241 \times 10^{14} \text{ cm}^{-3}, {}^7\text{Li}_1^I(t) = 0, t \geq 0 \quad (9)$$

A zero flux boundary condition is imposed along the  $\text{Li}_2\text{CO}_3/\text{Cu}$  interface, since Cu does not store  $\text{Li}^+$ .

After computing the dependence of  ${}^6\text{Li}_{2j-1}^I(t)$ ,  ${}^6\text{Li}_{2j}^L(t)$ ,  ${}^7\text{Li}_{2j-1}^I(t)$ , and  ${}^7\text{Li}_{2j}^L(t)$  on depth for a representative time, we obtain the isotope ratio  ${}^6\text{Li}^+/{}^7\text{Li}^+$  vs depth profile as

$$\begin{aligned} {}^6\text{Li}^+/{}^7\text{Li}^+ &= ({}^6\text{Li}_{2j-1}^I + {}^6\text{Li}_{2j}^L) / ({}^7\text{Li}_{2j-1}^I + {}^7\text{Li}_{2j}^L), \\ j &= 1, 2, 3, \dots, 40 \end{aligned} \quad (10)$$

Figure 4 compares the computed isotope ratio  ${}^6\text{Li}^+/{}^7\text{Li}^+$  vs depth profile at representative times from the (a) knock-off and (b) direct-hopping mechanisms in a  $\sim 20$  nm thick  $\text{Li}_2\text{CO}_3$  film. In both mechanisms,  ${}^6\text{Li}^+$  and  ${}^7\text{Li}^+$  can diffuse in to and out of the  $\text{Li}_2\text{CO}_3$  layer only via interstitial sites. Thus interstitials act like "channels" for  $\text{Li}^+$  diffusion, where the throughput of the channel is controlled by the equilibrium concentration of  $\text{Li}^+$ . The direct-hopping mechanism does not allow replacement of lattice  ${}^7\text{Li}^+$  with  ${}^6\text{Li}^+$ , so the ratio  ${}^6\text{Li}^+/{}^7\text{Li}^+$  cannot exceed the fraction of interstitials,  $\sim 10^{-8}$  ( $5.2 \times 10^{14} / 3.72 \times 10^{22}$ ). However, these few interstitials are relatively quickly replaced by  ${}^6\text{Li}^+$ —it takes only  $\sim 9.4$  s, as shown in Figure 4b. By contrast, the knock-off mechanism allows exchanges of lattice  ${}^7\text{Li}^+$  with interstitial  ${}^6\text{Li}^+$ . Considering that lattice  ${}^7\text{Li}^+$  must leave as the interstitial  ${}^6\text{Li}^+$  enters,  ${}^6\text{Li}^+/{}^7\text{Li}^+$  can become arbitrarily high in the knock-off mechanism. This gives rise to two characteristics shown in Figure 4: (1)  ${}^6\text{Li}^+/{}^7\text{Li}^+$  in the near surface layers is lower by 8 orders of magnitude with the direct-hopping mechanism than with the knock-off mechanism, and (2)  ${}^6\text{Li}^+/{}^7\text{Li}^+$  becomes saturated (flat) much more quickly with the direct-hopping mechanism because of the small number of ions ( ${}^7\text{Li}^+$  at the interstitial sites) that need to be replaced, even though the diffusion barrier is higher for the direct-hopping mechanism. The explanation for this situation can be seen from making an analogy of the diffusion process to the chemical reaction rate expression. In the direct-hopping mechanism, the interstitial  ${}^6\text{Li}^+$  travels via a first-order process, meaning an interstitial  ${}^6\text{Li}^+$  can jump at any time, without regard to its environment. However, in the knock-off mechanism, when interstitial  $\text{Li}^+$  jumps to a lattice site after a knock-off step, it

travels via a second-order reaction, meaning that a lattice  $\text{Li}^+$  cannot move until it is “replaced” by an interstitial  $\text{Li}^+$ . In the knock-off mechanism,  $\text{Li}^+$  becomes trapped at lattice sites while waiting to be replaced, thus greatly retarding the approach to a steady state. Nevertheless, it is important to keep in mind that, due to the extremely low concentration of interstitials, the overall  $^6\text{Li}^+$  flux that diffuses into  $\text{Li}_2\text{CO}_3$  from the direct-hopping mechanism is extremely low, and the knock-off mechanism allows much more  $^6\text{Li}^+$  to diffuse into  $\text{Li}_2\text{CO}_3$  than does the direct-hopping mechanism.

**3.4. Experimental Validation of the Two-Layer/Two-Mechanism SEI Diffusion Model.** The recent experimental study of Lu and Harris<sup>17</sup> suggests that SEI films grown on a Cu substrate consisting of two layers. One is a thin porous layer surrounded by electrolyte, and the other is a denser  $\sim 15$  nm thick layer which is predominantly  $\text{Li}_2\text{CO}_3$  or  $\text{Li}_2\text{O}$ . In the isotope exchange experiment,  $^6\text{LiBF}_4$  electrolyte provided the  $^6\text{Li}^+$ , while  $^7\text{Li}^+$  that was within the SEI film resulted from its preparation with a  $^7\text{LiClO}_4$  electrolyte. Results from TOF-SIMS measurements of isotope exchange within the SEI layers provided depth profiles of the isotope ratio  $^6\text{Li}^+/^7\text{Li}^+$  measured for three dipping times. The  $^6\text{Li}^+/^7\text{Li}^+$  eventually peaks at  $\sim 5$  nm inside the SEI rather than at the electrolyte/SEI interface: this supports the dual-layer model of the SEI film. Diffusion of  $\text{Li}^+$  must therefore occur by two different mechanisms, one through the porous layer and the other through the dense layer. While the diffusion mechanism in the porous layer can be easily modeled by Fick’s law, Lu and Harris<sup>17</sup> attributed diffusion through the denser layer to an unknown mechanism, which we have shown in this study to be the knock-off mechanism.

To validate the  $\text{Li}^+$  knock-off mechanism in the present study, fresh SEI films were grown following Lu and Harris.<sup>17</sup> With TEM, HRTEM, and XPS characterization, we demonstrate that crystalline  $\text{Li}_2\text{CO}_3$  is the main component of the dense inorganic (inner) layer of our synthesized SEI films. We then compare our predicted  $^6\text{Li}^+/^7\text{Li}^+$  depth profiles based upon solution of the knock-off diffusion eqs 5–7 with the Lu and Harris results.<sup>17</sup>

Figure 5a is a TEM image of one of our SEI films grown on Cu substrate with the Lu and Harris<sup>17</sup> method. Note that the bright region on the left is vacuum (i.e., no material) and the black region on the right is the Cu foil. Between these two are light and dark gray regions, with a net thickness in the 10–20 nm range, that may represent the porous organic (outer) and dense inorganic (inner) layers in the SEI film, respectively. The thickness of the porous organic layer could not be precisely determined here because it was broken and delaminated from the encapsulating epoxy during sample preparation. The HRTEM image in Figure 5b was acquired from the region highlighted by a dashed red square in Figure 5a. Nanosized ( $\sim 5$  nm) crystallites are seen in both layers. However, careful examination shows a preponderance of crystallites in the dark gray region relative to the light gray region, which has fewer crystallites and is likely semicrystalline (hence the contrast difference). Figure 5c shows an annularly integrated intensity plot from a diffractogram with reciprocal distance (or  $1/d$  in real space). This plot was obtained via fast Fourier transform of HRTEM images of one of the SEI films grown for this study. There are five peaks corresponding to the atomic plane spacings listed in the inset. The first and second peaks were indexed as (001) of  $\text{Li}_2\text{CO}_3$  and (111) of  $\text{Li}_2\text{O}$ . An XPS depth profile of the same SEI film is shown in Figure 5d. The substrate Cu profile (red) is taken from the  $\text{Cu}2p$  peak at 933 eV. The Cu profile shows that the thickness of the SEI film is not perfectly well-defined (due to low frequency surface roughness

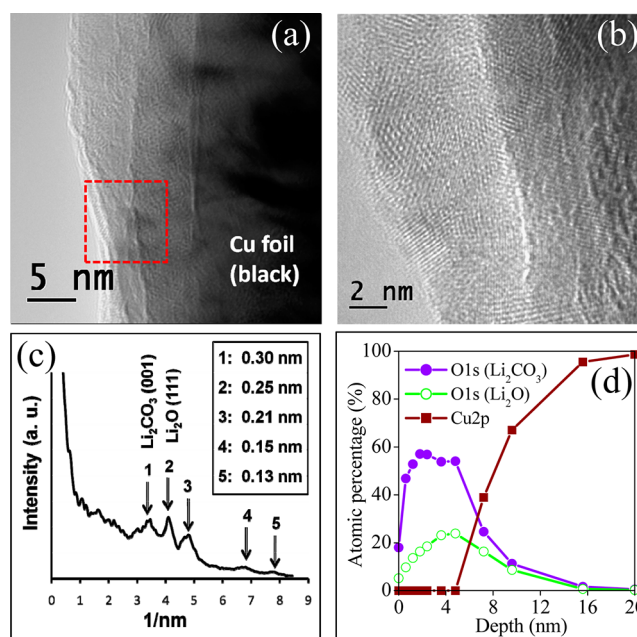


**Figure 5.** Evidence of the heterogeneous nature of the SEI growing on Cu substrate. (a) TEM image showing the SEI with two layers: outer layer (light gray) and inner layer (dark gray). (b) High-resolution TEM image acquired from an interfacial region between the outer and inner layers (highlighted by a dashed square in red) shows nanosized crystallites ( $\sim 5$  nm). (c) Profile of the annularly integrated intensity of a representative diffractogram of an HRTEM image taken from the inner layer vs reciprocal distance showing diffraction peaks in detail, where the first and second peaks were indexed as (001) of  $\text{Li}_2\text{CO}_3$  and (111) of  $\text{Li}_2\text{O}$ . (d) XPS depth profiles of  $\text{Li}_2\text{O}$ ,  $\text{Li}_2\text{CO}_3$ , and Cu.

components on Cu) but it extends to  $\sim 20$  nm, beyond which the primary species detected was Cu. The O1s peaks at 528.5 and 531.5 eV were selected to represent  $\text{Li}_2\text{O}$  and  $\text{Li}_2\text{CO}_3$ , respectively.<sup>21</sup> From the O1s depth profile, considerably more  $\text{Li}_2\text{CO}_3$  than  $\text{Li}_2\text{O}$  was observed in the SEI film. There is an obvious peak in the O1s profile (green) which belongs to  $\text{Li}_2\text{O}$  in Figure 5d at  $\sim 5$  nm. However, the fact that the same peak is not immediately apparent in the O1s ( $\text{Li}_2\text{CO}_3$ ) profile (blue) requires further interpretation. The peak in O1s ( $\text{Li}_2\text{CO}_3$ ) profile at  $\sim 2$  nm is due to the presence of  $\text{ROCO}_2\text{Li}$ ,  $\text{LiOH}$ , and other porous polymeric species.<sup>21,55</sup> We note that the  $\text{Li}_2\text{O}^+$  signal in the TOF-SIMS results from Lu and Harris (see Figure 2 in ref 17) could have resulted from either  $\text{Li}_2\text{CO}_3$  or  $\text{Li}_2\text{O}$ , but they can only be distinguished with XPS analysis. Hence, we conclude that the peak for the  $\text{Li}_2\text{CO}_3$  phase is coincident with the  $\text{Li}_2\text{O}$  ( $\sim 5$  nm) in Figure 5d since the peak at  $\sim 2$  nm is not solely representative of the  $\text{Li}_2\text{CO}_3$  phase.

Figure 6a contains results from TOF-SIMS depth profile measurements (open and filled symbols) from TOF-SIMS.<sup>17</sup> We use these results to further explore the diffusion mechanism of  $\text{Li}^+$  through the SEI. The depth profiles of both  $^6\text{Li}^+/^7\text{Li}^+$  (filled circles) and  $^{11}\text{B}^+$  (open circles) after immersing  $^7\text{Li}^+$  SEI in  $^6\text{LiBF}_4$  electrolyte for 15 min are shown. The  $^{11}\text{B}^+$  signal profile at the specimen surface quickly falls to the noise level over the outer  $\sim 5$  nm of SEI. This shows that the  $\sim 5$  nm outer layer of the  $^7\text{Li}^+$  SEI is porous and that a dense (i.e., nonporous) layer, comprised largely of  $\text{Li}_2\text{CO}_3$ , blocks the further diffusion of  $\text{BF}_4^-$  anions (indicated by  $^{11}\text{B}^+$ ). A higher value than natural abundance (8%) for the isotope ratio  $^6\text{Li}^+/^7\text{Li}^+$  demonstrates the incorporation of  $^6\text{Li}^+$  from  $^6\text{LiBF}_4$  electrolyte during the soaking process (in the

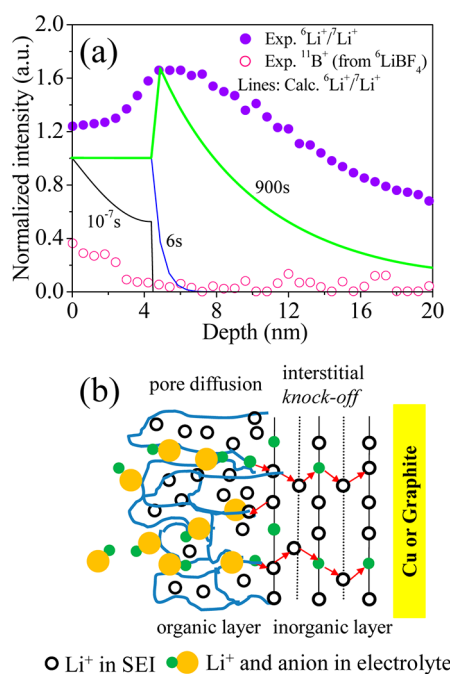


**Figure 6.** (a) TOF-SIMS measured (by the isotope exchange experiment) depth profiles of  ${}^6\text{Li}^+/{^7\text{Li}^+}$  and  ${}^{11}\text{B}^+$  (symbols) for the SEI growing on a Cu substrate after 900 s soaking and calculated depth profiles of  ${}^6\text{Li}^+/{^7\text{Li}^+}$  (solid lines) after  $10^{-7}$ , 6, and 900 s soaking. (b) Schematic drawing of pore diffusion in the porous organic layer of SEI and knock-off diffusion in the dense inorganic layer of SEI. The open circles represent the  $\text{Li}^+$  already in the SEI. In the porous organic layer, the blue solid lines denote channels through which  ${}^6\text{Li}^+$  in the electrolyte (green filled circles) transports with anions (yellow filled circles) via pore diffusion. The red arrows denote that only  $\text{Li}^+$  can diffuse in the dense inorganic layer via the knock-off mechanism.

absence of external electrical field). The isotope ratio  ${}^6\text{Li}^+/{^7\text{Li}^+}$  can therefore be used as a tracer for  ${}^6\text{Li}^+$  (from  ${}^6\text{LiBF}_4$  electrolyte) transport into the dense part of the SEI, which we take to be represented by  ${}^7\text{Li}_2\text{CO}_3$ . Unlike  $\text{BF}_4^-$ , the isotope ratio  ${}^6\text{Li}^+/{^7\text{Li}^+}$  is above the natural abundance level (8%) throughout the SEI film. More specifically, it first slowly increases, peaks at  $\sim 5$  nm, and then decreases through the dense layer toward the SEI/Cu interface. Since charge balance requires  $\text{BF}_4^-$  and  ${}^6\text{Li}^+$  to move together when they diffuse in pores, the discrepancy between the  ${}^{11}\text{B}^+$  and  ${}^6\text{Li}^+/{^7\text{Li}^+}$  trends in the dense SEI layer indicates that  ${}^6\text{Li}^+$  transports within the dense layer by a mechanism other than pore diffusion. In comparison, we performed similar measurements on crystalline  $\text{Li}_2\text{CO}_3$  film deposited on Cu substrate (see Supporting Information). No  $\text{BF}_4^-$  penetrated into  $\text{Li}_2\text{CO}_3$  film after 15 min of soaking. On the contrary, the  ${}^6\text{Li}^+/{^7\text{Li}^+}$  ratio keeps increasing with soaking time, confirming the knock-off mechanism. The  ${}^6\text{Li}^+/{^7\text{Li}^+}$  ratio profile is higher on the surface lower inside the film, similar to our simulation results in Figure 4a, clearly different from the results of real SEI with two layers.

As we previously demonstrated,  $\text{Li}^+$  diffusion in the dense  $\text{Li}_2\text{CO}_3$  layer is by  $\text{Li}_i^+$  via a knock-off mechanism. Figure 6b is a schematic illustration of our proposed two-layer/two-mechanism diffusion model of a SEI film in a Li-ion battery. The open circles represent the  $\text{Li}^+$  already in the SEI, i.e.,  ${}^7\text{Li}^+$ . In the porous layer, the blue solid lines denote channels through which  ${}^6\text{Li}^+$  (green filled circles) transports with anions from the electrolyte (yellow filled circles) via pore diffusion. The  ${}^7\text{Li}^+$  (open circles),

which are already part of the organic salt species that form the backbones of the porous layer, do not exchange with  ${}^6\text{Li}^+$ . In that case, the isotope ratio  ${}^6\text{Li}^+/{^7\text{Li}^+}$  in the porous region can never exceed the ratio of the number of  ${}^6\text{Li}^+$  ions in the electrolyte to the number of  ${}^7\text{Li}^+$  ions in the organic salt species. This ratio is suggested to be  $\sim 1$  by TOF-SIMS experiments.<sup>17</sup> The anion species ( $\text{BF}_4^-$ ) cannot diffuse into the dense layer due to its size. The dense layer is modeled as  $\text{Li}_2\text{CO}_3$  although in reality it is not exclusively  $\text{Li}_2\text{CO}_3$ . We propose that transport through the other species in the dense layer, which are mainly  $\text{Li}_2\text{O}$  and  $\text{LiF}$ , is likely to follow an analogous knock-off mechanism based on some theoretical predictions.<sup>52</sup> The red arrows denote  $\text{Li}^+$  (open circles) diffusion via knock-off in  $\text{Li}_2\text{CO}_3$ . Note also that some  $\text{Li}^+$  can diffuse from the dense layer back to the porous layer. The pore diffusion follows the 1D Fick's law, and the dense layer diffusion follows the knock-off diffusion equations (eqs 5–7).

Based on this two-layer/two-mechanism model, our computed concentration depth profiles at  $10^{-7}$ , 6, and 900 s (15 min) diffusion times are also included in Figure 6a as solid lines. Within  $10^{-7}$  s, the isotope ratio  ${}^6\text{Li}^+/{^7\text{Li}^+}$  penetrates only into the porous layer (black line). In fact, the  ${}^6\text{Li}^+/{^7\text{Li}^+}$  profile very quickly ( $\sim 4 \times 10^{-6}$  s) becomes constant in the  $\sim 5$  nm thick porous layer based on a typical diffusion coefficient of  $1 \times 10^{-6}$   $\text{cm}^2/\text{s}$  for  $\text{Li}^+$  in liquid electrolyte.<sup>16</sup> To emulate the Lu and Harris<sup>17</sup> experiments, we then set the isotope ratio  ${}^6\text{Li}^+/{^7\text{Li}^+}$  at the interface of the porous organic layer and the dense inorganic layer to be 1.75. This is reasonable since, in the isotope exchange experiment, the amount of electrolyte is not infinite but limited to a few droplets; hence, the  ${}^7\text{Li}^+$  will not maintain zero concentration as in the model formulated in section 3.3. From the knock-off diffusion mechanism, the isotope ratio  ${}^6\text{Li}^+/{^7\text{Li}^+}$  inside the dense layer increases with the soaking time, even after the  $\text{Li}^+$  concentration in the porous layer is already saturated. As expected with the knock-off mechanism in Figure 4a, the  ${}^6\text{Li}^+$  concentration exceeds the very small interstitial concentration and climbs up to a much higher isotope ratio  ${}^6\text{Li}^+/{^7\text{Li}^+}$  at a slower rate than the pore diffusion in the outer layer. Thus, the peak value of  ${}^6\text{Li}^+/{^7\text{Li}^+}$  inside the dense layer is lower than that in the porous layer at 6 s, but becomes higher than that in the porous layer at 900 s (15 min). The  ${}^6\text{Li}^+/{^7\text{Li}^+}$  depth profiles measured at different times by Lu and Harris<sup>17</sup> are between the computed 6 and 900 s results shown in Figure 6a. Thus, excellent agreement between theoretical and experimental profiles at 900 s is noted. The depth at which the isotope ratio  ${}^6\text{Li}^+/{^7\text{Li}^+}$  peaks, at the porous layer/dense layer interface, is well predicted by the knock-off diffusion model, as shown in Figure 6a. Note that experiment shows a gradually increasing isotope ratio  ${}^6\text{Li}^+/{^7\text{Li}^+}$  in the porous layer, since the boundary between the porous and dense regions is not perfectly sharp. We note that these results are in stark contrast to predictions from a homogeneous diffusion model, where the isotope ratio  ${}^6\text{Li}^+/{^7\text{Li}^+}$  profile would never climb within a uniform structure. With the knock-off mechanism in only one layer of  $\text{Li}_2\text{CO}_3$ , a higher ratio of  ${}^6\text{Li}^+/{^7\text{Li}^+}$  only occurs near the surface, not inside the film; this is shown in both Figure 4a and the Supporting Information.

The shape of the experimental isotope ratio  ${}^6\text{Li}^+/{^7\text{Li}^+}$  profile depends not only on variations in local SEI composition but also on the waiting time between the end of the soaking process and the time when the depth-profile measurements are conducted (about 12 h in this case). Self-diffusion will continue to flatten the  ${}^6\text{Li}^+/{^7\text{Li}^+}$  profile in each layer separately during the waiting time. The model does not consider the waiting time; it only predicts one limiting case.



For  $\text{Li}^+$  diffusion through a SEI film grown on a graphite electrode (for example) at low voltage, desolvation and electron-transfer processes at the electrolyte/SEI and SEI/graphite interfaces must also be considered. Nevertheless, the two-layer/two-mechanism diffusion model developed here can still be used to understand  $\text{Li}^+$  transport through the SEI. Due to the relatively small resistance of fresh SEI (see section 3.2), we estimate that the voltage drop across the SEI ( $\sim 2$  mV) should be too small to significantly impact the  $\text{Li}^+$  transport for modest currents.

Thus, instead of stopping the diffusion calculation at the SEI/Cu interface with a zero flux boundary condition, a semi-infinite graphite phase, in which  $\text{Li}^+$  diffuses according to the 1D direct-hopping mechanism can be added. With an initial condition of zero  $\text{Li}^+$  concentration, i.e.,  ${}^7\text{Li}_{2j+1}^i(0) = 0$ ,  ${}^6\text{Li}_{2j+1}^i(0) = 0$ ,  $j > 40$ , we can simulate  $\text{Li}^+$  diffusion across the SEI/graphite interface and diffusion into graphite. By solving the knock-off diffusion equations (eqs 5–7) in the dense  $\text{Li}_2\text{CO}_3$  layer of the SEI film and the direct-hopping equation in graphite, we find that a steady flow of  $\text{Li}^+$  into the graphite electrode occurs at  $\sim 1.92 \times 10^{-4}$  s, although the time to replace the lattice  $\text{Li}^+$  in  $\text{Li}_2\text{CO}_3$  is much longer. This means that to a first approximation, the SEI film acts as a chemically inert structure through which  $\text{Li}^+$  diffuses and where the transport rate is controlled primarily by the  $\text{Li}^+$  interstitial concentration in the dense layer. However, our results show that, on longer time scales, the SEI film becomes chemically involved (for example  $\text{Li}^+$  in electrolyte will replace the  $\text{Li}^+$  inside SEI). As we have shown earlier, the  $\text{Li}^+$  interstitial concentration can be changed by both temperature and voltage. In future studies, we shall consider the effects of doping  $\text{Li}_2\text{CO}_3$  with P (for example), which will increase interstitial concentration and thus may improve  $\text{Li}^+$  transport in the SEI.

#### 4. CONCLUDING REMARKS

Our theoretical calculations and TEM, HRTEM, XPS, and TOF-SIMS experiments suggest that the diffusion of  $\text{Li}_i^+$  in SEI films follows a two-layer/two-mechanism model.  $\text{Li}^+$  diffuses extremely rapidly in the porous organic layer, measured to be about 5 nm thick. In the dense inorganic layer, which experiments suggest to be predominantly crystalline  $\text{Li}_2\text{CO}_3$ , the  $\text{Li}_i^+$  is the dominant intrinsic defect, and  $\text{Li}_i^+$  diffuses via a repetitive knock-off with lattice  $\text{Li}^+$  sites within the (100) surface rather than via direct-hopping through the empty spaces between the lattice sites. The lower energy barrier for the knock-off mechanism is due to the stable coordination environment maintained during the process, where each  $\text{Li}^+$  coordinates with five O anions. The chemical basis for the knock-off mechanism could be generalized to all ionic conductors with isolated polyhedral anions or layered tetrahedral networks with interstitials as diffusion carrier. Numerical solutions of our two-layer/two-mechanism diffusion model successfully predict the unusual isotope ratio  ${}^6\text{Li}^+ / {}^7\text{Li}^+$  profile. This increases from the electrolyte/SEI interface through the porous layer, peaks at a depth of 5 nm, and then decreases beyond this point in the dense component which is primarily crystalline (monoclinic)  $\text{Li}_2\text{CO}_3$ . The SEI diffusion model directly predicts  $\text{Li}^+$  diffusion coefficients and  $\text{Li}^+$  concentration evolution: both are required by electrochemical cell modeling in order to predict the performance and life of a battery, but both are difficult to measure. The theoretical methods developed herein can be readily extended to study other materials in order to accelerate the design of artificial SEI or ionic conductors. In addition, we have developed a general multiscale diffusion modeling approach based upon insights acquired from DFT for direct comparison with isotope exchange diffusion measurements.

These constitute a framework from which ionic diffusion through multiple layer structures at nanoscale can be investigated and simulated.

#### ■ ASSOCIATED CONTENT

##### Supporting Information

Isotope exchange experiments on a pure, 700 nm thick  $\text{Li}_2\text{CO}_3$  crystalline film, providing further experimental evidence for the knock-off mechanism in  $\text{Li}_2\text{CO}_3$ . This material is available free of charge via the Internet at <http://pubs.acs.org>.

#### ■ AUTHOR INFORMATION

##### Corresponding Author

yue.qi@gm.com

##### Notes

The authors declare no competing financial interest.

#### ■ ACKNOWLEDGMENTS

The authors express their gratitude to Mr. Rui Wang for preparing  $\text{Li}_2\text{CO}_3$  thin film and Drs. Chen Li, Josh Campbell, and Mark Verbrugge for their careful review of the manuscript and insightful suggestions. The staff of the High Performance Computing Center at General Motors is acknowledged for computer hardware resources. Additional computational resources, networking, and support were provided by GM Information Systems and Services.

#### ■ REFERENCES

- (1) *Advances in lithium-ion batteries*; van Schalkwijk, W. A., Scrosati, B., Eds.; Kluwer: New York, 2002.
- (2) *Lithium-ion batteries: solid-electrolyte interphase*; Wang, Y., Balbuena, P. B., Eds.; Imperial College: London, 2004.
- (3) Xu, K. *Chem. Rev.* **2004**, *104*, 4303.
- (4) Aurbach, D.; Ein-Eli, Y.; Chusid, O.; Carmeli, Y.; Babai, M.; Yamin, H. *J. Electrochem. Soc.* **1994**, *141*, 603.
- (5) Aurbach, D.; Markovsky, B.; Shechter, A.; Ein-Eli, Y.; Cohen, H. *J. Electrochem. Soc.* **1996**, *143*, 3809.
- (6) Arora, P.; White, R. E.; Doyle, M. *J. Electrochem. Soc.* **1998**, *145*, 3647.
- (7) Wang, C.; Kakwan, I.; Appleby, A. J.; Little, F. E. *J. Electroanal. Chem.* **2000**, *489*, 55.
- (8) Zhang, J.; Wang, R.; Yang, X. C.; Lu, W.; Wu, X. D.; Wang, X. P.; Li, H.; Chen, L. W. *Nano Lett.* **2012**, *12*, 2153.
- (9) Winter, M. *Z. Phys. Chem.* **2009**, *223*, 1395.
- (10) Tarascon, J. -M.; Armand, M. *Nature* **2001**, *414*, 359.
- (11) Armand, M.; Tarascon, J. -M. *Nature* **2008**, *451*, 652.
- (12) Peled, E. *J. Electrochem. Soc.* **1979**, *126*, 2047.
- (13) Xu, K.; von Cresce, A.; Lee, U. *Langmuir* **2010**, *26*, 11538.
- (14) Peled, E.; Golodnitsky, D.; Ardel, G. *J. Electrochem. Soc.* **1997**, *144*, L208.
- (15) Christensen, J.; Newman, J. *J. Electrochem. Soc.* **2004**, *151*, A1977.
- (16) Borodin, O.; Smith, G. D.; Fan, P. *J. Phys. Chem. B* **2006**, *110*, 22773.
- (17) Lu, P.; Harris, S. J. *Electrochem. Commun.* **2011**, *13*, 1035.
- (18) Mizusaki, J.; Tagawa, H.; Saito, K.; Uchida, K.; Tezuka, M. *Solid State Ionics* **1992**, *53–56*, 791.
- (19) Dollé, M.; Grugeon, S.; Beaudoin, B.; Dupont, L.; Tarascon, J. -M. *J. Power Sources* **2001**, *97–98*, 104.
- (20) Shim, J.; Kostecki, R.; Richardson, T.; Song, X.; Striebel, K. A. *J. Power Sources* **2002**, *112*, 222.
- (21) Verma, P.; Maire, P.; Novák, P. *Electrochim. Acta* **2010**, *22*, 6332.
- (22) Kresse, G.; Furthmüller, J. *Phys. Rev. B* **1996**, *54*, 11169.
- (23) Blöchl, P. E. *Phys. Rev. B* **1994**, *50*, 17953.
- (24) Ceperley, D. M.; Alder, B. J. *Phys. Rev. Lett.* **1980**, *45*, 566.
- (25) Perdew, J. P.; Zunger, A. *Phys. Rev. B* **1981**, *23*, 5048.
- (26) Leslie, M.; Gillan, M. J. *J. Phys. C: Solid State Phys.* **1985**, *18*, 973.

- (27) Idemoto, Y.; Richardson, J. W.; Koura, N.; Kohara, S.; Loong, C. K. *J. Phys. Chem. Solids* **1998**, *59*, 363.
- (28) Parlinski, K.; Li, Z. Q.; Kawazoe, Y. *Phys. Rev. Lett.* **1997**, *78*, 4063.
- (29) Duan, Y.; Sorescu, D. C. *Phys. Rev. B* **2009**, *79*, 014301.
- (30) Henkelman, G.; Uberuaga, B. P.; Jonsson, H. *J. Chem. Phys.* **2000**, *113*, 9901.
- (31) Perdew, J. P.; Burke, K.; Ernzerhof, M. *Phys. Rev. Lett.* **1996**, *77*, 3865.
- (32) Iddir, H.; Curtiss, L. A. *J. Phys. Chem. C* **2010**, *114*, 20903.
- (33) Chen, Y. C.; Ouyang, C. Y.; Song, L. J.; Sun, Z. L. *J. Phys. Chem. C* **2011**, *115*, 7044.
- (34) Zhang, S. B.; Northrup, J. E. *Phys. Rev. Lett.* **1991**, *67*, 2339.
- (35) Lee, E. C.; Chang, K. J. *Phys. Rev. B* **2004**, *70*, 115210.
- (36) Verbrugge, M. W.; Baker, D. R.; Koch, B. J. *J. Power Sources* **2002**, *110*, 295.
- (37) Dahn, J. R. *Phys. Rev. B* **1991**, *44*, 9170.
- (38) Islam, M. M.; Bredow, T.; Minot, C. *J. Phys. Chem. B* **2006**, *110*, 9413.
- (39) Levi, M. D.; Wang, C.; Aurbach, D. *J. Electrochem. Soc.* **2004**, *151*, A781.
- (40) *Defects in Solid*; Tilley, R. J. D., Ed.; Wiley: New York, 2008.
- (41) Fahey, P. M.; Griffin, P. B.; Plummer, J. D. *Rev. Mod. Phys.* **1989**, *61*, 289.
- (42) One of these metastable structures, with  $\text{Li}_i^+$  at  $T_m$  in Figure 3b, corresponds to the metastable interstitial site  $T_m$  discussed in Figure 1. We believe this to be the starting structure in the literature,<sup>32</sup> since the energy difference between our transition state and the structure at  $T_m$  is 0.326 eV. This is very close to the energy barrier of 0.28 eV reported in the literature.<sup>32</sup>
- (43) Markovsky, B.; Rodkin, A.; Cohen, Y. S.; Palchik, O.; Levi, E.; Aurbach, D.; Kim, H. J.; Schmidt, M. *J. Power Sources* **2003**, *119–121*, 504.
- (44) Geronov, Y.; Schwager, F.; Muller, R. H. *J. Electrochem. Soc.* **1982**, *129*, 1422.
- (45) Churikov, A. V. *Electrochim. Acta* **2001**, *46*, 2415.
- (46) Schranzhofer, H.; Bugajski, J.; Santner, H. J.; Korepp, C.; Möller, K. C.; Besenhard, J. O.; Winter, M.; Sitte, W. *J. Power Sources* **2006**, *153*, 391.
- (47) Seitz, F. *Acta Crystallogr.* **1950**, *3*, 355.
- (48) Heitjans, P.; Tobschall, E.; Wilkening, M. *Eur. Phys. J. Special Topics* **2008**, *161*, 97.
- (49) Kimura, N.; Greenblatt, M. *Mater. Res. Bull.* **1984**, *19*, 1653.
- (50) Du, Y. A.; Holzwarth, N. A. W. *Phys. Rev. B* **2007**, *76*, 174302.
- (51) Hodge, I. M.; Ingram, M. D.; West, A. R. *J. Am. Ceram. Soc.* **1976**, *59*, 360.
- (52) Gavartin, J. L.; Catlow, C. R. A.; Shluger, A. L.; Varaksin, A. N.; Kolmogorov, Y. N. *Modell. Simul. Mater. Sci. Eng.* **1992**, *1*, 29.
- (53) Sheppard, L. R.; Atanacio, A. J.; Bak, T.; Nowotny, J.; Prince, K. E. *J. Phys. Chem. B* **2007**, *111*, 8126.
- (54) King, J. R.; Sharp, T. E.; Tuck, B.; Rogers, T. G. *Proc. R. Soc. London A* **1995**, *450*, 623.
- (55) Aurbach, D. *J. Power Sources* **2000**, *89*, 206.

## Supporting Information

### Direct Calculation of Li-ion Transport in the Solid Electrolyte Interphase

Siqi Shi<sup>1,5</sup>, Peng Lu<sup>2</sup>, Zhongyi Liu<sup>3</sup>, Yue Qi<sup>3,\*</sup>,  
Louis G. Hector, Jr.<sup>3</sup>, Hong Li<sup>4</sup>, Stephen J. Harris<sup>3</sup>

<sup>1</sup>*School of Engineering, Brown University, Providence, RI 02912, USA*

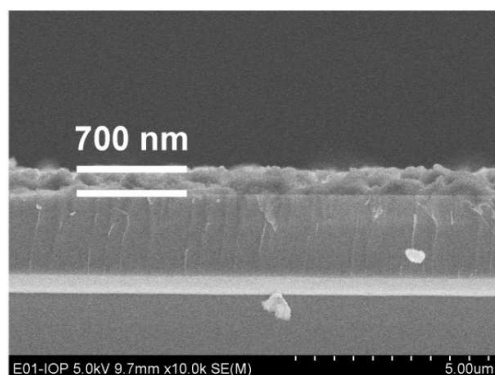
<sup>2</sup>*Trison Business Solutions Inc., 17 Bank Street, Le Roy, NY 14482, USA*

<sup>3</sup>*General Motors R&D Center, Warren, MI 48090, USA*

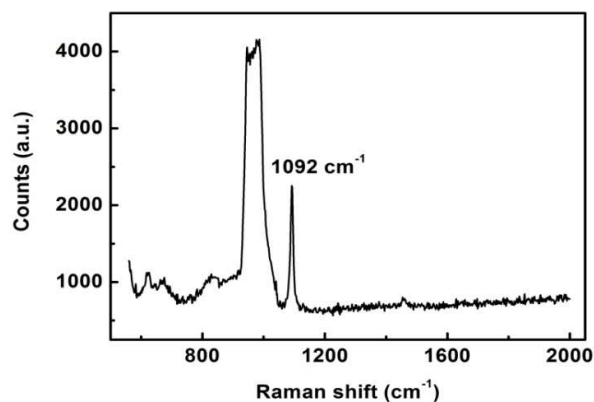
<sup>4</sup>*Institute of Physics, Chinese Academy of Sciences, Beijing, 100190, China*

<sup>5</sup>*Department of Physics, Zhejiang Sci-Tech University, Hangzhou 310018, China*

To provide further experimental evidence for the knock-off mechanism in  $\text{Li}_2\text{CO}_3$ , we performed isotope exchange experiments on a pure, 700 nm-thick  $\text{Li}_2\text{CO}_3$  crystalline film, deposited on a flat Si substrate via an RF-sputtering method. The Si substrate was chosen since we were not interested in forming SEI, which requires a conductive substrate (like Cu). A pure  $\text{Li}_2\text{CO}_3$  pellet was used as the target. The  $\text{Li}_2\text{CO}_3$  was deposited under 1 Pa Ar for 3 hours at 60 W. Figure S1 (a) is an SEM image that shows a cross-section of the  $\text{Li}_2\text{CO}_3$  film on the Si substrate. The  $1092\text{ cm}^{-1}$  peak in the Raman spectrum of Fig. S1(b) provides clear evidence for crystalline  $\text{Li}_2\text{CO}_3$ .



(a)



(b)

Figure S1 (a) SEM cross sectional image of a 700nm-thick  $\text{Li}_2\text{CO}_3$  thin film deposited on a Si substrate. (b) Raman spectrum of the film in (a) clearly shows the  $\text{Li}_2\text{CO}_3$  peak at  $1092\text{cm}^{-1}$ .



The measured  ${}^6\text{Li}^+/{^7\text{Li}^+}$  isotope ratio in the deposited  $\text{Li}_2\text{CO}_3$  thin film was 0.12; this is the same as its ratio in natural abundance. Following a 15min soak in  ${}^6\text{LiBF}_4$  electrolyte, the amount of  $\text{BF}_4^-$  that penetrated into the  $\text{Li}_2\text{CO}_3$  film was measured to be nearly zero. As Fig. S2 shows, however, the  ${}^6\text{Li}^+/{^7\text{Li}^+}$  from TOF-SIMS measurements increases with soaking time. This demonstrates that the  ${}^6\text{Li}^+$  from the electrolyte exchanges positions with the  ${}^7\text{Li}^+$  in the deposited  $\text{Li}_2\text{CO}_3$  film, and confirms the *knock-off* mechanism for  $\text{Li}^+$  diffusion within the  $\text{Li}_2\text{CO}_3$  film. The highest  ${}^6\text{Li}^+/{^7\text{Li}^+}$  occurs right at the  $\text{Li}_2\text{CO}_3$ /electrolyte interface (rather than inside the SEI film). This feature is consistent with the *knock-off* mechanism shown in Fig. 4(a), and is further confirmation that the unique  ${}^6\text{Li}^+/{^7\text{Li}^+}$  profile in SEI must be explained by the two-layer/two-mechanism diffusion model.

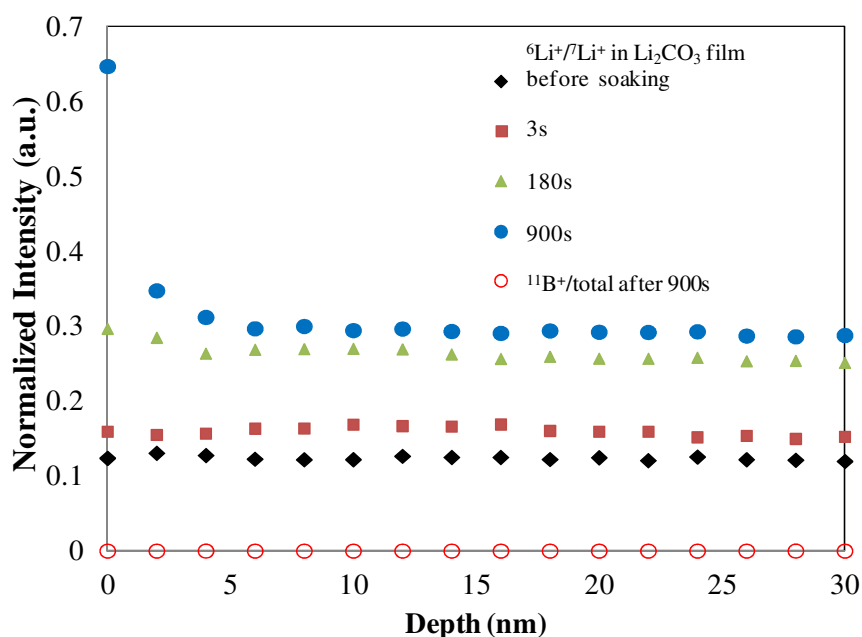


Figure S2. Depth profiles of  ${}^6\text{Li}^+/{^7\text{Li}^+}$  and  ${}^{11}\text{B}^+$  (symbols) through the  $\text{Li}_2\text{CO}_3$  film deposited on a Si substrate after different soaking time. Experimental data generated with TOF-SIMS following the Lu and Harris [1] isotope exchange experiment.

## References

- [1] Lu, P.; Harris, S. J. *Electrochem. Commun.* **2011**, *13*, 1035.